

The catalytic diversity of zeolites: confinement and solvation effects within voids of molecular dimensions

Cite this: *Chem. Commun.*, 2013, **49**, 3491

Rajamani Gounder and Enrique Iglesia*

The ability of molecular sieves to control the access and egress of certain reactants and products and to preferentially contain certain transition states while excluding others based on size were captured as shape selectivity concepts early in the history of zeolite catalysis. The marked consequences for reactivity and selectivity, specifically in acid catalysis, have since inspired and sustained many discoveries of novel silicate frameworks and driven the engineering of hierarchical structures and void size to influence catalysis. The catalytic diversity of microporous voids is explored and extended here in the context of their solvating environments, wherein voids act as hosts and stabilize guests, whether reactive intermediates or transition states, by van der Waals forces. We use specific examples from acid catalysis, including activation of C–C and C–H bonds in alkanes, alkylation and hydrogenation of alkenes, carbonylation of dimethyl ether, and elimination and homologation reactions of alkanols and ethers, which involve transition states and adsorbed precursors of varying size and composition. Mechanistic interpretations of measured turnover rates enable us to assign precise chemical origins to kinetic and thermodynamic constants in rate equations and, in turn, to identify specific steps and intermediates that determine the free energy differences responsible for chemical reactivity and selectivity. These free energy differences reflect the stabilization of transition states and their relevant precursors *via* electrostatic interactions that depend on acid strength and van der Waals interactions that depend on confinement within voids. Their respective contributions to activation free energies are examined by Born–Haber thermochemical cycles by considering plausible transition states and the relevant precursors. These examples show that zeolite voids solvate transition states and precursors differently, and markedly so for guest moieties of different size and chemical composition, thus enabling voids of a given size and shape to provide the “right fit” for a given elementary step, defined as that which minimizes Gibbs free energies of activation. Tighter confinement is preferred at low temperatures because enthalpic gains prevail over concomitant entropic losses, while looser fits are favored at high temperatures because entropy gains offset losses in enthalpic stabilization. Confinement and solvation by van der Waals forces are not directly involved in the making or breaking of strong chemical bonds; yet, they confer remarkable diversity to zeolites, in spite of their structural rigidity and their common aluminosilicate composition. A single zeolite can itself contain a range of local void environments, each with distinct reactivity and selectivity; as a result, varying the distribution of protons among these locations within a given framework or modifying a given location by partial occlusion of the void space can extend the range of catalytic opportunities for zeolites. Taken together with theoretical tools that accurately describe van der Waals interactions between zeolite voids and confined guests and with synthetic protocols that place protons or space-filling moieties at specific locations, these concepts promise to broaden the significant impact and catalytic diversity already shown by microporous solids.

Received 28th January 2013,
Accepted 4th March 2013

DOI: 10.1039/c3cc40731d

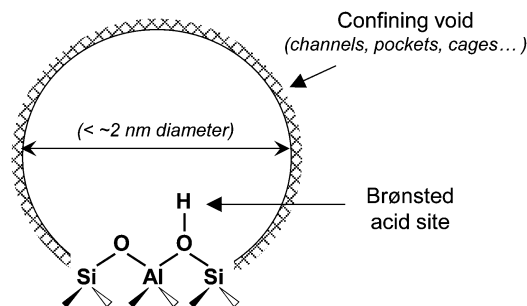
www.rsc.org/chemcomm

1. Introduction

Zeolites are microporous crystalline inorganic oxides used widely as solid Brønsted acid catalysts to mediate chemical

reactions relevant in the synthesis of fuels, energy carriers, and petrochemicals.^{1–5} Reactive intermediates and transition states involved in the elementary steps that mediate acid-catalyzed reactions are cationic species stabilized by electrostatic and covalent interactions with the conjugate anions of the acid sites. These species are also stabilized by non-specific van der Waals interactions when the confining microporous oxide structures

Department of Chemical Engineering, University of California at Berkeley, Berkeley, CA 94720, USA. E-mail: iglesiasia@berkeley.edu; Fax: +1 510 642 4778



Scheme 1 Two-dimensional representation of a zeolitic active site, comprised of Brønsted acid sites that are similar in acid strength and of confining void environments that vary in size and topology.

are of molecular dimensions ($< \sim 2$ nm). Thus, zeolitic active sites are defined both by the hydroxyl groups that act as Brønsted acids and by surrounding microporous cavities (Scheme 1) that solvate confined species involved in catalytic cycles. In spite of their modest conformational flexibility and limited compositional diversity, zeolitic active sites resemble in structure and function the active sites in biological catalysts, which consist of catalytic centers held within pockets lined with amino acid residues that solvate substrates and transition states largely *via* non-covalent interactions.^{6–8} Here, we discuss how electrostatic and dispersion forces depend on zeolite void structure and composition and how they stabilize confined transition states and intermediates and, in this manner, influence the dynamics of elementary steps within catalytic sequences.

We begin in Section 2 by providing evidence that active sites in microporous aluminosilicates are similar in acid strength but are remarkably diverse in void structure and in their solvation of confined species through van der Waals interactions. In Sections 3 and 4, we interpret turnover rates for several elimination and addition reactions of organic molecules using mechanism-derived rate equations, which rigorously assign chemical significance to measured rate constants and allow describing the dynamics of chemical reactions using free energy differences between the kinetically-relevant transition states and the relevant reactive intermediates. These examples show that zeolites influence catalytic rates or selectivities when a transition state is solvated differently than the relevant reactive intermediates or than any other transition states, respectively. We conclude by discussing strategies that seek to

design or select zeolites differing in catalytic function as a result of the solvation properties of their confining voids, which contrast and complement alternate approaches that do so based solely on heuristic size exclusion principles.

2. Zeolitic active sites: the effects of void structure on acid strength and solvation properties

Structural and compositional differences among active sites in zeolites reflect concomitant differences in either the acid sites or the voids that confine them (Scheme 1). Brønsted acid sites differ in composition and strength when framework Si atoms are replaced by different trivalent cations (*e.g.*, Al, Fe, Ga, B);⁹ among zeolites, which are strictly aluminosilicates, acid sites differ in local structure and geometric arrangement when Al atoms are present at different crystallographically-distinct framework tetrahedral sites (T-sites).^{10,11} Intrazeolite void volumes relevant in descriptions of the catalytic behavior of these acid sites depend on both the steric constraints enforced by the crystalline framework and on the spatial requirements or “activation volume”¹² for a given chemical reaction. These structural and compositional heterogeneities cause differences in the free energies of confined intermediates and transition states, leading to catalytic rates and selectivities that vary among zeolite frameworks and even among different void locations that exist within a single framework.

2.1. Acid strength and its weak dependence on void structure for isolated sites in aluminosilicates

The electrostatic stabilization of intermediates and transition states depends on acid strength to an extent that reflects the amount and diffuseness of their positive charge.^{13,14} Brønsted acid strength is rigorously expressed as the deprotonation energy (DPE), defined as the energy required to separate a proton (H^+) from the conjugate base (XO^-) to non-interacting distances. These DPE values are accessible to density functional theory (DFT) calculations for acids of known structure. DPE values for zeolitic acids are estimated imprecisely by available DFT methods that treat solids as periodic structures, in spite of the well-defined atomic arrangements in such materials; they are estimated more precisely by combined quantum mechanical and interatomic potential calculations (QM-Pot), which account for long-range electrostatic interactions in periodic

Rajamani Gounder received his BS in Chemical Engineering from the University of Wisconsin in 2006 and his PhD in Chemical Engineering from the University of California, Berkeley in 2011 under the guidance of Professor Iglesia. He received the Heinz Heinemann Award for Graduate Research in Catalysis and the Berkeley Campus Outstanding Graduate Student Instructor Award in 2010 in recognition of his research and teaching accomplishments at Berkeley. Upon completion of his current postdoctoral stay with Professor Mark E. Davis at the California Institute of Technology, he will join the School of Chemical Engineering at Purdue University as an Assistant Professor.

Enrique Iglesia is the Theodore Vermuelen Chair in Chemical Engineering at the University of California, Berkeley and a Faculty Senior Scientist in the E. O. Lawrence Berkeley National Laboratory. He received his PhD in Chemical Engineering in 1982 from Stanford University and joined the Berkeley faculty in 1993 after eleven years at the Corporate Research Labs of Exxon. He is the President of the North American Catalysis Society and the former Editor-in-Chief of Journal of Catalysis. His research group studies the synthesis and structural and mechanistic characterization of inorganic solids useful as catalysts for chemical reactions important in energy conversion, petrochemical synthesis, and environmental control.

structures more accurately than DFT methods alone.¹⁵ DPE values do not depend on the stability of the base that ultimately accepts the proton in a given catalytic sequence and thus reflect solely the properties of the solid acid.

In contrast with DPE values, interaction enthalpies of bases with protons are inaccurate probes of acid strength because they depend on electrostatic stabilization of the ion-pair,¹⁶ which is influenced by charge delocalization within the protonated base, and on van der Waals stabilization of the protonated base by the confining voids,^{17,18} which depends on their respective sizes. These inaccuracies are evident in pyridine adsorption enthalpies that are more negative in smaller H-MFI channels (-200 ± 5 kJ mol⁻¹; ~ 0.55 nm void diameter) than in larger H-FAU supercages (-180 ± 5 kJ mol⁻¹; ~ 1.3 nm void diameter),¹⁹ in spite of their similar DPE values estimated by QM-Pot methods.¹⁵ They are also evident in the similar adsorption enthalpies of ammonia (-145 ± 5 kJ mol⁻¹ for both) and pyridine (-200 and -195 ± 5 kJ mol⁻¹, respectively)^{17,20} on H⁺ sites of different strength in Al- and Fe-substituted MFI zeolites (DPE values are higher in Fe-MFI by >20 kJ mol⁻¹).^{21–23} NH₃ adsorption at isolated framework Al sites in zeolites has been simulated using grand canonical ensemble Monte Carlo (GCMC) methods that treat atomic interaction potentials as additive Lennard-Jones and coulombic potentials.²⁴ These treatments have shown that electrostatic interactions between NH₃ and OH groups are similar in FAU, FER, MFI and MOR, but that confinement of NH₃ within these voids cause differences in adsorption energies (up to ~ 20 kJ mol⁻¹).²⁴ The similar NH₃ protonation energies on isolated zeolitic acid sites,²⁴ together with measured turnover rates of *n*-C₆H₁₄ cracking on MFI^{25–27} and of iso-C₈H₁₈ cracking on FAU^{28,29} that were also unaffected by Al framework density, led to inferences about the similar strength of isolated protons among zeolites of very diverse void structures in the early literature.

The definition of DPE implies that acid strength differences must reflect differences in stability between XO–H species and the deprotonated conjugate anions (XO⁻). The stability of deprotonated conjugate anions in zeolites reflect the ability of [AlO₄]⁻ tetrahedra in various framework structures and T-sites to accept and delocalize the negative charge. QM-Pot calculations show that conjugate anion structures are nearly identical in energy (within 5 kJ mol⁻¹) among the four distinct Al T-sites in MOR.³⁰ DPE values vary over a slightly wider range than [AlO₄]⁻ stabilities because they also reflect the stabilities of covalent XO–H bonds; yet, they are similar among the different T-sites in CHA (within ~ 6 kJ mol⁻¹),³¹ MFI (within ~ 10 kJ mol⁻¹)³² and MOR (within ~ 18 kJ mol⁻¹).³⁰ DPE values for the most stable T-site locations in different aluminosilicates are also similar (within ~ 30 kJ mol⁻¹; CHA, FAU, MFI, MOR)³⁰ and fall within a narrower range than those for silica frameworks substituted with Al, B, Fe, or Ga heteroatoms, which vary by more than 80 kJ mol⁻¹.^{21–23,33} QM-Pot calculations show that DPE values for FAU zeolites (1161–1166 kJ mol⁻¹) are essentially independent of Al framework density and increase only when another Al atom is present at next nearest neighbor locations (1177–1247 kJ mol⁻¹).³⁴ Also, DPE values among

zeolitic acid sites do not correlate with Si–O–Al bond angles^{30,32} or O–H bond lengths,³¹ or with spectroscopic signatures, such as OH infrared vibrational frequencies³¹ or ¹H NMR chemical shifts.^{30,32} Thus, differences in local structure do not seem to significantly influence the delocalization of the negative charge at [AlO₄]⁻ tetrahedra isolated within an insulating SiO₂ framework.

In contrast with high-silica zeolites of similar acid strength (DPE ~ 1170 – 1200 kJ mol⁻¹),³⁰ Keggin-type tungsten polyoxometalate (POM) clusters (H_{8–*n*}X^{*n*+}W₁₂O₄₀; H_{8–*n*}XW) contain acid sites that are stronger and more diverse in strength (DPE ~ 1050 – 1150 kJ mol⁻¹),^{35,36} in part, because the conjugate anions of reducible oxides with semiconducting properties can delocalize negative charge more effectively than those of insulating oxides.³⁷ DPE values for W-based POM clusters increase systematically (1067–1143 kJ mol⁻¹)³⁸ with decreasing central atom valence (S⁶⁺, P⁵⁺, Si⁴⁺, Al³⁺, Co²⁺) and with the concomitant increase in the number of charge-balancing protons. Moreover, DPE values of residual H⁺ sites on H₃PW (1087 kJ mol⁻¹) increase upon the protonation of adsorbed species (~ 1090 – 1175 kJ mol⁻¹), which requires the delocalization of additional negative charge left behind within conjugate anions upon proton transfer.³⁶ Thus, residual acid sites weaken (and DPE values increase) in response to the presence of other protons or protonated species on semiconducting oxide clusters, resulting in 2-butanol protonation enthalpies that become less negative with increasing DPE (Fig. 1).³⁶ Although W-based POM acids (DPE ~ 1050 – 1150 kJ mol⁻¹)^{35,36} are stronger than high-silica zeolitic acids (DPE ~ 1170 – 1200 kJ mol⁻¹)³⁴ when their surfaces are uncovered, POM acids become comparatively weaker at high adsorbate coverages because more negative charge in conjugate anions becomes delocalized throughout the POM cluster. We conclude that the insulating properties of silica frameworks cause acid strength, and its effect on the electrostatic stabilization of ion-pairs at isolated

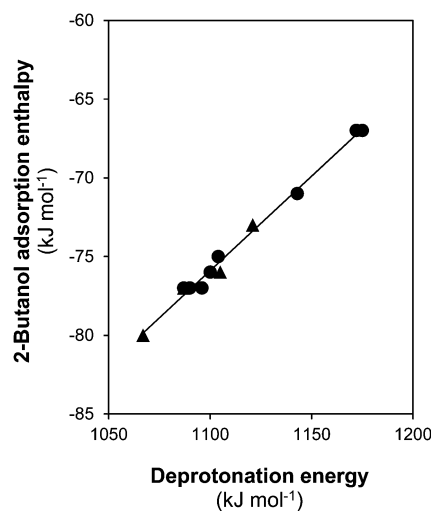


Fig. 1 2-Butanol adsorption enthalpies on Keggin-type tungsten polyoxometalate clusters as a function of DPE, which varies with central atom (\blacktriangle ; S⁶⁺, P⁵⁺, Si⁴⁺, Al³⁺) and in the presence of other adsorbed bases (\bullet ; H₂O, 2-C₄H₉OH, pyridine, 2,6-di-*tert*-butylpyridine). Data originally reported by Janik *et al.*³⁶

$[\text{AlO}_4]^-$ centers, to vary only weakly among different zeolites and among different T-sites within a given framework. Yet, as we discuss next, the structural and topological diversity of microporous voids, and their effects on the solvation of confined species, confer significant catalytic diversity to highly siliceous acidic zeolites.

2.2. Solvation properties and their strong dependence on the confining void structure

The catalytic differences among isolated protons at various framework locations reflect predominantly the structural differences of the local confining voids, which stabilize molecules by van der Waals forces, and of the connecting apertures, which control the access and egress of reactants and products. The extent to which guest molecules are solvated by confining voids reflects, in turn, the number of host-guest contacts and the strength of the van der Waals interactions between them, which depends on the chemical identity of the atoms and functional groups in the guest complexes and on their distances from the framework oxygens in the host voids. Attractive van der Waals interactions between lone pairs in framework oxygens and polarizable electron clouds in inert gases (*e.g.*, Ar, Xe)^{39–42} strengthen as the confining space becomes smaller (until molecules no longer fit and Pauli repulsion dominates), causing perturbations in ¹²⁹Xe NMR chemical shifts and in Ar adsorption energies. Adsorption enthalpies become more negative for hydrocarbons,^{43–50} alkanols,^{51–53} and ammonia²⁴ with decreasing void size and increasing molecular size (again, up to the point of size exclusion), as shown in Fig. 2 for C₃H₈ adsorbed in channels of H-FER (~0.40–0.46 nm diameter), H-MFI (~0.51–0.63 nm diameter) and H-MOR (12-MR channels).^{44–46} These stronger van der Waals interactions also lead to more negative adsorption entropies (Fig. 2), because of the ubiquitous compensation between enthalpies and entropies, brought forth by the loss of mobility

as confinement becomes tighter and the host-guest contacts become more effective.^{45,46,48,50,54}

The effects of confinement on the enthalpies and entropies of stable molecules also influence those of transient species along reaction coordinates, such as the ion-pair transition states that mediate acid-catalyzed reactions. Monomolecular alkane activation (Scheme 2) involves the quasi-equilibrated adsorption of gaseous alkanes (A) on intrazeolitic protons without charge transfer^{44–46} (K_{ads} ; alkane adsorption equilibrium constant), followed by the kinetically-relevant protonation of alkane C–C or C–H bonds (k_{int} ; intrinsic rate constant) in cracking or dehydrogenation events, respectively. These reactions prevail on zeolitic acids at high temperatures (>623 K) and low pressures of alkane reactants and alkene products.⁵⁵ Such conditions lead to dilute intrazeolite alkane concentrations ($C_{\text{A}(z)}$) and to sparsely covered H⁺ sites,⁵⁶ and alkane activation turnover rates (per H⁺) that are first-order in alkane pressure (P_{A}):

$$r = k_{\text{int}}C_{\text{A}(z)} = k_{\text{int}}K_{\text{ads}}P_{\text{A}} = k_{\text{meas}}P_{\text{A}} \quad (1)$$

where k_{meas} is the measured first-order rate constant. The normalization of alkane activation turnover rates (eqn (1)) by either the reactant concentration within zeolitic voids ($C_{\text{A}(z)}$) or the extrazeolite gaseous reactant pressure (P_{A}) give k_{int} and k_{meas} values, respectively:

$$k_{\text{int}} = r/C_{\text{A}(z)} \quad (2)$$

$$k_{\text{meas}} = r/P_{\text{A}} \quad (3)$$

These thermodynamic (K_{ads}) and kinetic (k_{int} , k_{meas}) constants reflect Gibbs free energy differences between the reactants, intermediates and transition states depicted in Scheme 2. The solvation properties of voids, which do not influence the free energy of protons ($\Delta G_{\text{H}^+Z}^0$), influence K_{ads} values only *via* free energy differences between confined ($\Delta G_{\text{A}(z)}^0$) and gaseous alkanes ($\Delta G_{\text{A}(g)}^0$) (Scheme 2):

$$K_{\text{ads}} = \exp\left(-\left(\Delta G_{\text{A}(z)}^0 - \Delta G_{\text{A}(g)}^0 - \Delta G_{\text{H}^+Z}^0\right)/RT\right) \quad (4)$$

Similarly, solvation properties influence k_{int} and k_{meas} *via* free energy differences between confined transition states (ΔG_{\ddagger}^0) and either confined or gaseous alkanes, respectively (Scheme 2):

$$k_{\text{int}} = (k_{\text{B}}T/h) \exp\left(-\left(\Delta G_{\ddagger}^0 - \Delta G_{\text{A}(z)}^0\right)/RT\right) \quad (5)$$

$$k_{\text{meas}} = (k_{\text{B}}T/h) \exp\left(-\left(\Delta G_{\ddagger}^0 - \Delta G_{\text{A}(g)}^0 - \Delta G_{\text{H}^+Z}^0\right)/RT\right) \quad (6)$$

Intrinsic and measured alkane activation rate constants (eqn (5) and (6)) reflect the free energy of the *same* confined transition state relative to that of either a confined or an unconfined alkane in ΔG_{int} and ΔG_{meas} , respectively (Scheme 2).⁵⁶

The free energy differences in eqn (4)–(6) can be dissected into their enthalpy and entropy components to give corresponding differences among enthalpies and entropies of gaseous or confined alkanes and monomolecular transition states. Intrinsic (E_{int}) and measured (E_{meas}) activation energies reflect

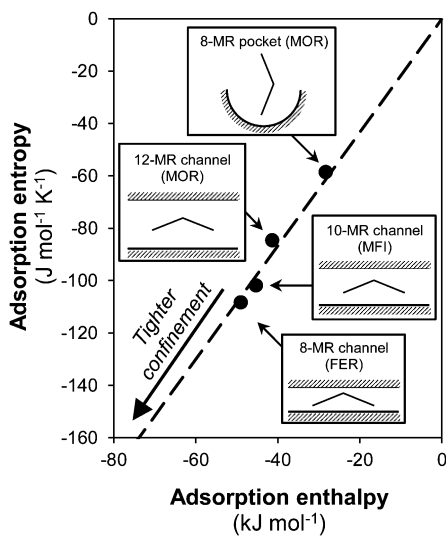
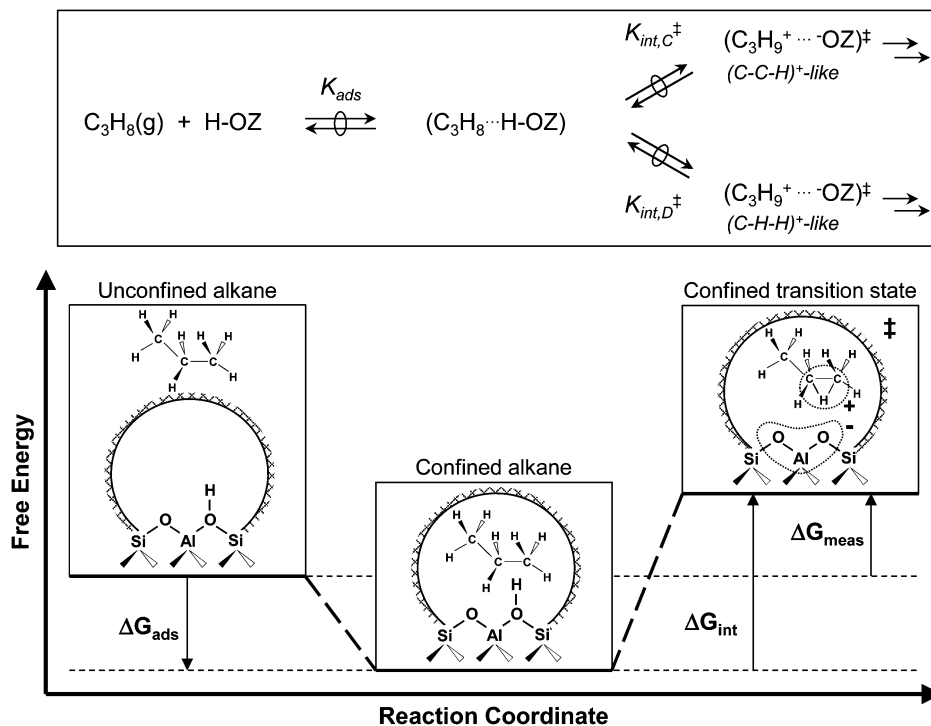


Fig. 2 Adsorption enthalpies and entropies for propane reported by Eder *et al.*^{44–46} on H-FER (8-MR channels), H-MFI (10-MR channels) and H-MOR (12-MR channels) and estimated for 8-MR H-MOR side pockets (details in Section 3.2).



Scheme 2 Reaction scheme for monomolecular alkane activation (shown for C_3H_8 using transition state theory formalism), involving quasi-equilibrated alkane adsorption from the gas phase (g) onto Brønsted acid sites (H–OZ) located within zeolite voids (z), and kinetically-relevant cracking or dehydrogenation steps mediated by carbonium-ion-like transition states ($C_3H_9^+$). Gibbs free energy versus reaction coordinate diagram for alkane cracking shows that measured (k_{meas}) and intrinsic (k_{int}) rate constants reflect free energy differences between the same confined transition state and either unconfined (ΔG_{meas}) or confined alkane reactants (ΔG_{int}).

the enthalpy of confined transition states relative to that of confined or unconfined alkanes, respectively. These two activation energies differ by the alkane adsorption enthalpy (ΔH_{ads}):

$$E_{meas} = E_{int} + \Delta H_{ads} \quad (7)$$

As we discuss next, Born–Haber thermochemical cycles can separate these activation barriers into enthalpy differences that independently reflect reactant and catalyst properties,^{57,58} thus allowing changes in E_{int} and E_{meas} values with alkane and zeolite structure to be ascribed to changes in specific steps within the thermochemical cycle and to the underlying effects of acid strength and solvation on these steps. These rigorous thermochemical cycle formalisms provide insights about how electrostatic and van der Waals forces stabilize cationic transition states and uncharged reactants in monomolecular alkane activation catalytic sequences.

2.3. Thermochemical cycles: interpreting the effects of acid strength and solvation on monomolecular alkane activation barriers

Scheme 3 shows a thermochemical cycle that relates measured activation energies for monomolecular alkane activation to the individual energies of its elementary steps (Scheme 2) and to those for hypothetical steps that connect reactants with the kinetically-relevant transition state. After deprotonation of the acid, the gaseous proton is placed at a C–C (or C–H) bond in a gaseous alkane to form the gaseous analog of the cationic transition state formed in cracking (or dehydrogenation) steps.

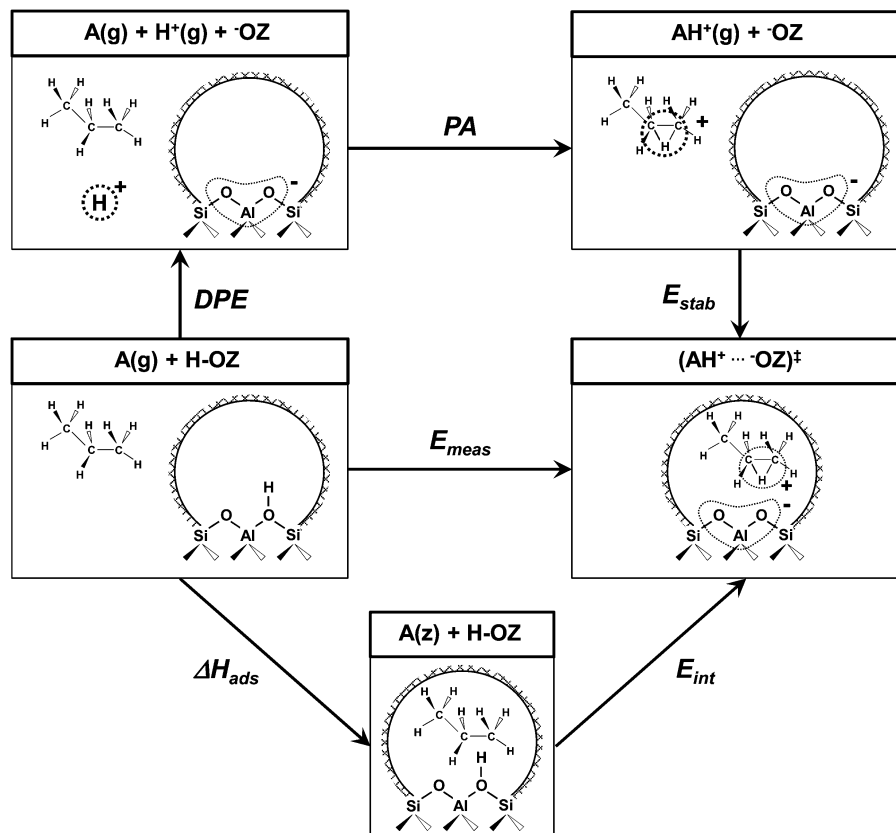
The proton affinities (PA) of C–C and C–H bonds in alkanes correspond to the energies of proton addition to form loosely-bound van der Waals complexes, in which the neutral fragment (the smaller alkane or the H_2 product in cracking or dehydrogenation, respectively) and the carbenium ion interact.^{59–62} These gaseous complexes structurally resemble the late ion-pair transition states found in theoretical studies of monomolecular cracking and dehydrogenation of C_2 – C_4 alkanes on small zeolite clusters (3–5 T-atoms).^{63–66} In the final step of this thermochemical cycle, gaseous transition state analogs become confined within zeolite voids, where they are stabilized by electrostatic interactions with the conjugate $[AlO_4]^-$ anions and by van der Waals interactions with framework oxygens; their combined effects give the stabilization energy (E_{stab}). E_{meas} and E_{int} values are given by the sum of energies for the hypothetical steps in the thermochemical cycle (Scheme 3) that connect the relevant alkane precursor and the transition state:

$$E_{int} = DPE + PA + E_{stab} \quad (8)$$

$$E_{meas} = DPE + PA + E_{stab} - \Delta H_{ads} \quad (9)$$

In this cycle (Scheme 3), DPE values depend only on catalyst properties, PA values depend only on reactant properties, E_{stab} values depend on properties of both catalysts and transition states, and ΔH_{ads} values depend on catalyst and reactant properties.

Measured and intrinsic monomolecular cracking barriers⁶⁷ and adsorption enthalpies^{45,46} of C_3 – C_6 *n*-alkanes on H-MFI are



Scheme 3 Thermochemical cycle for monomolecular alkane (A) activation reactions (shown for C_3H_8 cracking) at zeolitic acid sites (H-OZ). Measured activation energies (E_{meas}) depend on alkane adsorption enthalpies (ΔH_{ads}) and intrinsic protonation barriers (E_{int}) corresponding to the elementary steps in Scheme 2. E_{meas} values are also given by the sum of acid site deprotonation energies (DPE), gas-phase alkane proton affinities (PA), and stabilization energies upon confinement of gaseous cations within zeolite voids (E_{stab}).

shown in Fig. 3. These E_{meas} values were determined from the temperature dependence of the total cracking rate of each reactant, given by the sum of individual C-C bond cracking rates. Thus, these E_{meas} values are reactivity-weighted and predominantly reflect cracking of central C-C bonds (in C_{4+} n -alkanes); for example, turnover rates (per C-C bond; 773 K) of n - C_6H_{14} cracking on H-MFI are larger by factors of ~ 5 for central than for terminal C-C bonds.⁶⁷ Differences in reactivity-weighted E_{meas} values for different n -alkanes on the same zeolite, for which DPE terms cancel rigorously in eqn (8), therefore reflect solely the differences in reactivity-weighted PA and E_{stab} values.

E_{meas} values for cracking of C_3 - C_6 n -alkanes on H-MFI vary over a wide range (105 - 155 kJ mol^{-1})⁶⁷ and decrease monotonically with increasing alkane carbon number (~ 15 kJ mol^{-1} per CH_2 group; Fig. 3). Gas-phase reaction enthalpies of proton-mediated n -alkane cracking to form a smaller alkane and carbenium-ion, which corresponds to the protonation step in the thermochemical cycle (Scheme 3), are similar (within ~ 10 kJ mol^{-1} , estimated by DFT or MP2) for the three outermost C-C bonds in n - $C_{10}H_{22}$ chains.⁶⁸ These similar reaction enthalpies, in turn, indicate that reactivity-weighted PA values are similar among C_3 - C_6 n -alkanes. Thus, E_{meas} values decrease systematically (~ 15 kJ mol^{-1} per CH_2 group; Fig. 3) with increasing n -alkane chain length because the E_{stab} terms also decrease systematically, reflecting an increase in the number of

van der Waals contacts with pore walls as transition states (and reactants) become larger.

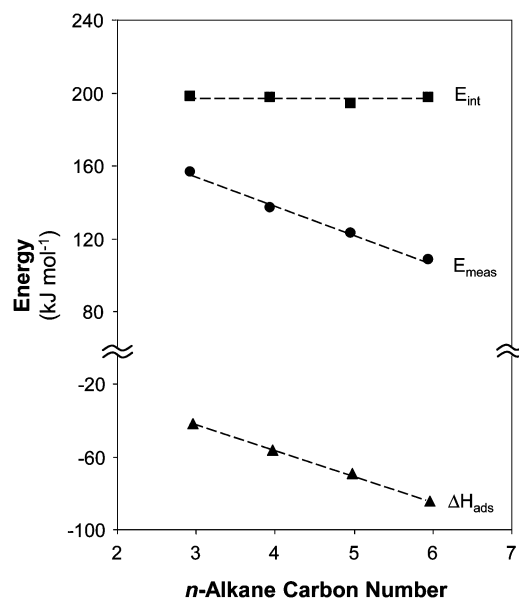


Fig. 3 Measured activation energies (●), reactant adsorption enthalpies (▲) and intrinsic activation energies (■) for monomolecular cracking of C_3 - C_6 n -alkanes on H-MFI. Adapted from Gounder *et al.*,⁷⁰ data originally reported by Eder *et al.*^{45,46,67}

Table 1 Measured (E_{meas}) and intrinsic (E_{int}) activation energies for monomolecular propane cracking and propane adsorption enthalpies (ΔH_{ads}) on acidic zeolites. E_{int} values calculated from E_{meas} and ΔH_{ads} values reported in the literature and eqn (7)

Zeolite	MOR	MOR	MOR	FER	MFI	USY	MFI	MFI	MOR	BEA	FAU	MFI	MWW
E_{meas}	160 ^a	167 ^a	160 ^a	157 ^a	158 ^a	165 ^d	155 ^e	147 ^f	147 ^f	158 ^f	165 ^f	164 ^h	160 ^h
ΔH_{ads}	-41 ^b	-41 ^b	-41 ^b	-49 ^c	-45 ^b	-31 ^b	-45 ^b	-45 ^b	-41 ^b	-39 ^g	-31 ^b	-45 ^b	-49 ⁱ
E_{int}	201	208	201	206	203	196	200	192	188	197	196	209	209

^a Data from Gounder *et al.*⁵⁶ ^b Data from Eder *et al.*⁴⁶ ΔH_{ads} values for MOR correspond to 12-MR MOR channels; ΔH_{ads} values for FAU correspond to supercage voids. ^c Data from Eder *et al.*⁴⁴ ^d Data from Gounder *et al.*⁷⁰ ^e Data from Narbeshuber *et al.*⁶⁷ ^f Data from Xu *et al.*⁷² ^g Estimated from correlation between ΔH_{ads} values for MOR and BEA reported by Denayer *et al.*⁴⁸ assuming a ΔH_{ads} value of $-41.3 \text{ kJ mol}^{-1}$ for C_3H_8 in MOR. ^h Data from Liu *et al.*⁷¹ ⁱ Data from He *et al.*⁷³

In contrast with *measured* activation energies, *intrinsic* activation barriers for C_3 – C_6 *n*-alkane cracking on H-MFI depend only weakly on chain length (194 – 198 kJ mol^{-1} ; Fig. 3),⁶⁷ as also reported for larger *n*-alkanes (C_3 – C_{20}).^{25,69} The nearly invariant reactivity-weighted PA values with chain length imply, in turn, that the weak dependence of E_{int} on carbon number must reflect a similar insensitivity of the $(E_{\text{stab}} - \Delta H_{\text{ads}})$ term in eqn (9) to the length of *n*-alkane chains. Adsorption enthalpies in H-MFI become systematically more negative with increasing *n*-alkane chain size (by $\sim 12 \text{ kJ mol}^{-1}$ per CH_2 group; Fig. 3) because of the larger number of van der Waals contacts between reactants and the confining voids.^{45,46} Stabilization enthalpies of gaseous monomolecular transition states upon confinement (E_{stab} ; *via* E_{meas} , eqn (8)) also become more negative as *n*-alkane size increases (by $\sim 15 \text{ kJ mol}^{-1}$ per CH_2 group; Fig. 3), because these ion-pairs are similar in size and composition to the alkane reactant and are stabilized to similar extents by van der Waals forces.^{54,63} E_{meas} values, which depend only on E_{stab} (eqn (8)), are sensitive to the solvating properties of voids because enthalpies of confined ion-pairs are *referenced to those of unconfined gaseous alkanes* (Scheme 2). E_{int} values, which depend on both E_{stab} and ΔH_{ads} terms (eqn (9)), are much less sensitive to the solvation of transition states because *the relevant reactants are confined alkanes* that are solvated to a similar extent by van der Waals forces (Scheme 2).

The strength of solvation interactions depends on the size and composition of the confined moieties (*e.g.*, C_3 – C_6 *n*-alkanes in H-MFI) and also on the size and shape of the confining voids (*e.g.*, C_3H_8 in different H-zeolites). The effects of solvation, however, are only evident in activation barriers when they reflect enthalpy differences between transition states and reactants that are *solvated to different extents*. Intrinsic activation barriers for monomolecular C_3H_8 cracking on several zeolites (BEA, FAU, FER, MFI, MOR, MWW; void diameter ~ 0.4 – 1.3 nm), estimated from E_{meas} values measured in our group^{56,70} and other laboratories^{67,71,72} and from ΔH_{ads} values measured by calorimetric and chromatographic methods,^{44,46,48,73} are remarkably similar ($199 \pm 11 \text{ kJ mol}^{-1}$; Table 1), in spite of the very different void structures of these materials. The weak dependence of E_{int} on void size is even more evident for monomolecular cracking of *n*- C_6H_{14} on FAU, MFI and MOR zeolites (differ by $\leq 10 \text{ kJ mol}^{-1}$), for which ΔH_{ads} and E_{meas} varied over much larger ranges (36 and 37 kJ mol^{-1} , respectively).⁷⁴ The similar E_{int} values for cracking of the same alkane on different zeolites, given the identical PA and similar DPE values in eqn (9), reflect similarities among the remaining

$(E_{\text{stab}} - \Delta H_{\text{ads}})$ term in eqn (9), as expected from the nearly commensurate solvation of monomolecular transition states and reactant alkanes upon confinement.

The similar size and composition of dehydrogenation and cracking transition states for a given alkane ($(\text{C}_n\text{H}_{2n+3})^+$) should also lead to their similar solvation by any given zeolite void. *n*-Alkane dehydrogenation and cracking transition states differ primarily in the proton location (at C–H or C–C bonds, respectively). Mulliken charge analysis indicates that both ion-pairs ($+0.8$ – $0.9 e$) have the positive charge localized at the C-atom that ultimately connects the alkoxide intermediate to a framework O-atom,^{11,63,75,76} suggesting that electrostatic interactions would also be similar between each of these cationic transition states and a given conjugate $[\text{AlO}_4]^-$ anion. Thus, $E_{\text{stab,C}}$ and $E_{\text{stab,D}}$ terms are similar and cancel in differences between dehydrogenation and cracking activation energies on the same zeolite (eqn (8)):

$$E_{\text{meas,D}} - E_{\text{meas,C}} = (\text{DPE}_D + \text{PA}_D + E_{\text{stab,D}}) - (\text{DPE}_C + \text{PA}_C + E_{\text{stab,C}}) \quad (10)$$

The rigorous cancellation of the zeolite-dependent DPE term in eqn (10) indicates, in turn, that differences in measured dehydrogenation and cracking activation energies on the same zeolite predominantly reflect the affinity of the gaseous alkane for protonation at its C–H and C–C bonds to form the gaseous analogs of the two transition states:

$$E_{\text{meas,D}} - E_{\text{meas,C}} = \text{PA}_D - \text{PA}_C \quad (11)$$

Dehydrogenation and cracking activation energies for C_3H_8 , *n*- C_4H_{10} , and iso- C_4H_{10} have been reported on FER, MFI, MOR and FAU (void diameters ranging from ~ 0.4 – 1.3 nm).^{56,70,77} Activation energies for alkane dehydrogenation reflect reactivity-weighted values for dehydrogenation of individual C–H bonds, because alkene isomers interconvert *via* facile double-bond and skeletal isomerization at the temperatures required for alkane activation ($>700 \text{ K}$).^{56,77} In contrast, activation energies for the cracking of specific C–C bonds can be determined because they form smaller and less reactive alkanes (rates decrease ~ 10 -fold per carbon number).⁷⁸

Differences between dehydrogenation and cracking activation energies (from total cracking rates) for each alkane on various zeolites are shown in Fig. 4 as a function of the difference between their mean C–H and C–C bond proton affinities, calculated by weighting PA values for each C–H and C–C bonds (estimated by *ab initio* theoretical treatments)^{60–62}

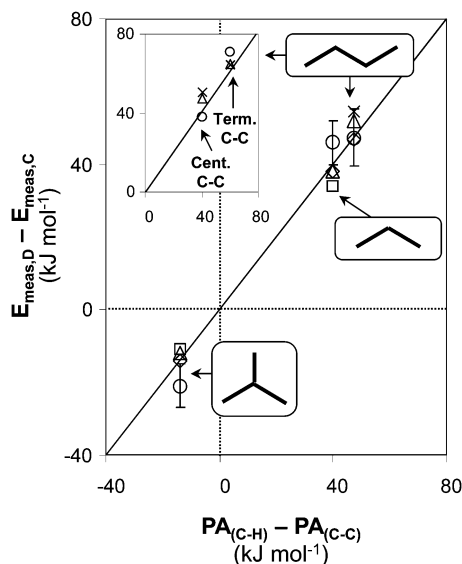


Fig. 4 Difference between measured activation energies (E_{meas}) for mono-molecular alkane dehydrogenation and cracking on H-MOR (\diamond), H-MFI (\circ), H-FER (Δ), H-USY (\square) and CD-HUSY (\boxtimes) plotted against the difference in gas-phase C-H and C-C proton affinities (PA) of propane, *n*-butane, and iso-butane (details in Section 2.3). Error bars shown for MFI are representative of errors for all samples. eqn (11) plotted as solid line. Inset: differences between E_{meas} values for dehydrogenation of *n*-butane and those for cracking at its terminal or central C-C bonds. Adapted from Gounder *et al.*⁷⁰

by the number of such bonds in each reactant.⁷⁰ For $n\text{-C}_4\text{H}_{10}$, the differences between $E_{\text{meas,D}}$ values and the individual $E_{\text{meas,C}}$ values for terminal and central C-C bond cleavage are also shown in the inset of Fig. 4; these activation energy differences are plotted against the differences in PA between an average C-H bond and either the terminal or central C-C bond in $n\text{-C}_4\text{H}_{10}$.⁷⁰ For each alkane reactant, differences in dehydrogenation and cracking barriers fall (within experimental error) on the parity line defined by eqn (11) (Fig. 4), indicating that they predominantly reflect proton affinity differences between C-H and C-C bonds in gaseous alkanes. Activation barriers are higher for dehydrogenation than for cracking of C_3H_8 by $\sim 40 \text{ kJ mol}^{-1}$ on all zeolites (Fig. 4),^{56,70,71} in contrast with earlier studies, which have reported C_3H_8 dehydrogenation barriers ranging from 60 kJ mol^{-1} lower to 10 kJ mol^{-1} higher than C_3H_8 cracking barriers on MFI zeolites.^{67,72,79} The higher barriers for C_3H_8 dehydrogenation than cracking (by $\sim 40 \text{ kJ mol}^{-1}$; Fig. 4) are indeed expected from eqn (11) and from gaseous $(\text{C-H-H})^+$ -like cations that are less stable than $(\text{C-C-H})^+$ -like cations (by $\sim 40 \text{ kJ mol}^{-1}$).^{60,70}

The differences between dehydrogenation and cracking barriers for each alkane reactant are similar on zeolites with a wide range of void diameters ($\sim 0.4\text{--}1.3 \text{ nm}$; Fig. 4), reflecting the similar solvation of dehydrogenation and cracking ion-pairs within a given void by van der Waals forces (*via* E_{stab}). We conclude from these findings (Fig. 4), together with the weak dependence of cracking E_{int} values on *n*-alkane size (Fig. 3) and void structure (Table 1), that van der Waals forces within a given void lead to a similar enthalpic stabilization of confined guests that are similar in size and composition.

3. Consequences of void structure for catalytic reactivity: preferential solvation of transition states over kinetically-relevant reactants

In this section, we discuss how voids of varying size and structure cause differences in turnover rates when transition states and reactants are solvated differently upon confinement. The ability to probe different void environments within a given framework requires methods that can locate protons, as well as synthetic protocols that can place them within specific locations during or after synthesis. In the latter case, this involves the use of titrants that access sites only at certain locations or thermochemical treatments that remove protons from certain locations. We begin with a brief discussion of the catalytic behavior of MFI zeolites, a material uniquely prominent in the history of zeolite catalysis, but for which precise and reliable methods to locate Al atoms or OH groups remain unavailable. We then focus on the catalytic behavior of MOR zeolites, a structure containing OH groups located within two distinctly different void environments, which can be distinguished by infrared (IR) spectroscopy.

3.1. Alkane activation rates on MFI: inextricable contributions to reactivity from acid sites present at several locations within a given zeolite framework

MFI zeolites contain Al atoms sited at 24 unique framework T-sites (in the monoclinic form) with corresponding OH groups distributed among void structures defined by straight and sinusoidal 10-MR channels ($\sim 0.51\text{--}0.56 \text{ nm}$ diameter)⁸⁰ and their intersections ($\sim 0.63 \text{ nm}$ diameter, determined by the largest inscribed sphere).⁸¹ C_3H_8 cracking and dehydrogenation turnover rates (748 K; per H^+) vary by up to a factor of ~ 10 (Table 2) among MFI samples of different provenance and

Table 2 Measured rate constants for monomolecular propane cracking ($k_{\text{meas,C}}$) and dehydrogenation ($k_{\text{meas,D}}$) at 748 K and *n*-hexane cracking alpha test values (α) at 811 K on H-MFI zeolites of varying Al content

Zeolite	Si/Al ratio	$k_{\text{meas,C}}$ ($10^{-3} \text{ mol (mol H}^+)^{-1} \text{ s}^{-1} \text{ bar}^{-1}$)	$k_{\text{meas,D}}$ ($10^{-3} \text{ mol (mol H}^+)^{-1} \text{ s}^{-1} \text{ bar}^{-1}$)	α ($10^5 \text{ (mol Al)}^{-1}$)
H-MFI ^a	16.5	6.3	3.9	—
H-MFI ^a	19	2.0	2.1	—
H-MFI ^a	25	4.4	3.5	—
H-MFI ^a	40	1.5	0.8	—
H-MFI ^b	43	1.1	1.05	—
H-MFI (3D0m-i) ^b	64	0.57 ^c	0.35 ^c	—
H-MFI (pillared) ^b	71	0.88 ^c	0.50 ^c	—
H-MFI ^d	21	—	—	2.8
H-MFI ^d	37	—	—	3.1
H-MFI ^d	70	—	—	2.7
H-MFI ^d	110	—	—	2.9
H-MFI ^d	240	—	—	1.7

^a Data from Gounder *et al.*⁵⁶ ^b Data from Liu *et al.*⁷¹ 3D0m-i and pillared denote mesoporous/microporous structures synthesized by imprinting onto three-dimensionally ordered mesoporous carbon, and by pillaring methods, respectively. ^c Rate constants normalized by the number of H^+ sites in microporous voids, reported in Table 6 of Liu *et al.*⁷¹ ^d Data from Fig. 2 in Olson *et al.*²⁷

Si/Al ratios (15–70).^{56,71} These turnover rate differences may reflect different distributions of Al among the unique T-sites in MFI, which vary in the geometry of the surrounding space, but not in acid strength.³² At first glance, these inferences about site heterogeneity in MFI materials seem inconsistent with earlier studies,^{25–27} which reported that *n*-C₆H₁₄ cracking rates (811 K; per Al) varied less than two-fold (Table 2) among H-MFI samples prepared *via* similar protocols but with different Si/Al ratios (20–240). These data led to the proposal of equivalent reactivity among all T-sites in MFI,^{26,27} but they could reflect instead a similar Al distribution among all T-sites in these samples conferred by their similar synthesis protocols,^{82–84} as also noted by these authors.²⁵

New insights into these seemingly inconsistent inferences regarding the catalytic heterogeneity of Al sites in MFI would require precise methods to characterize Al or OH location. Multiple quantum MAS NMR spectroscopy can resolve distinct ²⁷Al isotropic chemical shifts to within 0.2 ppm, yet these chemical shifts cannot be assigned unequivocally to specific T-site locations in MFI because some chemical shifts differ by values smaller than the uncertainties in theoretical estimates (*e.g.*, 13 of the 24 T-sites are within a 3.5 ppm range).^{83,84} Fluorescence spectra of zeolite single crystals (>~1 nm diameter) using X-ray standing waves can identify Al atoms at specific framework T-sites,⁸⁵ providing an option to study the catalytic consequences of Al location on MFI single crystals. The detection of distinct framework Al sites appears more tractable than the detection of individual OH groups in MFI, because the latter (48 unique O atoms in monoclinic MFI) have similar IR vibrational frequencies and are contained within voids of similar size,⁸⁶ in contrast with MOR zeolites, as we discuss next.

3.2. Alkane activation rates on MOR zeolites: distinct contributions from acid sites within two different void environments

MOR frameworks contain only 4 T-sites and OH groups located within either large 12-MR channels (~0.70 nm diameter) or smaller, shallow 8-MR pockets (~0.41 nm diameter, ~0.37 nm depth).⁸⁷ Large titrants (*e.g.*, pyridine, 2,6-lutidine, *n*-hexane) can only access 12-MR MOR channels at ambient temperatures (~303 K),⁸⁷ causing OH IR spectra to show a persistent band centered at ~3592 cm⁻¹ for 8-MR OH groups at saturation coverages of these titrants.^{87–90}

MOR samples with similar Al density but of different provenance exhibit different OH distributions (Table 3),⁵⁶ which can be determined by deconvolution of their IR bands into 8-MR (~3592 cm⁻¹) and 12-MR (~3611 cm⁻¹) components.⁸⁷ These findings indicate that Al siting in MOR depends on variables that are seldom controlled during synthesis, at least in part because the challenges in determining Al location and in recognizing its dramatic catalytic consequences have been articulated only recently.^{12,56,77,87,91} Protocols to site Al atoms at specific locations during MOR synthesis remain unavailable, but the selective replacement of H⁺ in 8-MR side pockets with monovalent alkali cations (*e.g.*, Na⁺; Table 3) enables post-synthetic modifications of OH distributions.^{87,89,92}

Table 3 Elemental composition and OH distribution between 8-MR pockets and 12-MR channels of H-MOR zeolites; adapted from Gounder *et al.*⁵⁶

Zeolite	Source	Si/Al ratio	Na/Al ratio	OH _{8-MR} (%)	OH _{12-MR} (%)
H ₁₀₀ Na ₀ -MOR-T	Tosoh	8.9	0.001	78	22
H ₁₀₀ Na ₀ -MOR-S	Sud-Chemie	10.1	0.001	60	40
H ₁₀₀ Na ₀ -MOR-Z	Zeolyst	10.0	0.001	56	44
H ₈₃ Na ₁₇ MOR-Z	Zeolyst	10.0	0.17	36	64
H ₇₃ Na ₂₇ MOR-Z	Zeolyst	10.0	0.27	27	73
H ₅₉ Na ₄₁ MOR-Z	Zeolyst	10.0	0.41	20	80
H ₄₅ Na ₅₅ MOR-Z	Zeolyst	10.0	0.55	13	87

Alkane interactions with zeolitic active sites predominantly reflect van der Waals interactions with framework oxygens, which weaken as void diameters increase, as well as weak induced-dipole interactions with OH groups, the strength of which is independent of the confining void structure.^{44–46} As a result, propane adsorption enthalpies ($\Delta H_{\text{ads}} = -49, -45$ and -41 kJ mol⁻¹) and entropies ($\Delta S_{\text{ads}} = -108, -102$ and -85 J mol⁻¹ K⁻¹) become systematically less negative as void diameter increases (Fig. 2) among H-FER (~0.40–0.46 nm), H-MFI (~0.51–0.63 nm) and H-MOR (~0.70 nm for 12-MR channels).^{44–46} Adsorption equilibrium constants (at 323 K) for a given *n*-alkane increase systematically as void size decreases and adsorption enthalpies become more negative,^{44–46} in spite of the concomitant losses in entropy upon tighter confinement. At low temperatures, alkane adsorption is driven predominantly by enthalpy instead of entropy factors, because contributions of entropy to free energy are weighted by temperature in the defining equation:

$$\Delta G = \Delta H - T\Delta S \quad (12)$$

Calorimetric, gravimetric and infrared studies have shown that C₃₊ *n*-alkanes adsorb within larger 12-MR MOR channels (~0.70 nm diameter) instead of 8-MR MOR pockets (~0.41 nm diameter) at low temperatures (323 K).⁴⁶ This preference suggests that adsorption of C₃₊ *n*-alkanes is more exothermic, and van der Waals contacts are more effective, in 12-MR MOR channels than in 8-MR side pockets, an observation inconsistent with their relative void diameters. Dispersion interactions, however, also become weaker as spatial constraints prevent effective van der Waals contacts between confined guests and pore walls. Indeed, geometric considerations indicate that 8-MR MOR side pockets are too shallow (~0.37 nm in depth) to fully contain C₃₊ *n*-alkanes (>0.65 nm in length), precluding effective van der Waals contacts between 8-MR framework oxygens and all CH_x moieties in the alkane; these contacts provide the enthalpic driving force relevant for adsorption at low temperatures.⁵⁶

Monomolecular alkane activation occurs at much higher temperatures (700 K) than adsorption measurements (<350 K), resulting in stronger contributions from entropy terms to free energies (eqn (12)).⁷⁰ Turnover rates (per H⁺) for cracking (Fig. 5a) and dehydrogenation (Fig. 5b) of propane, *n*-butane and iso-butane increased systematically with increasing fraction of H⁺ sites within 8-MR MOR pockets; these rates were below detection limits for dehydrogenation of C₃H₈ and

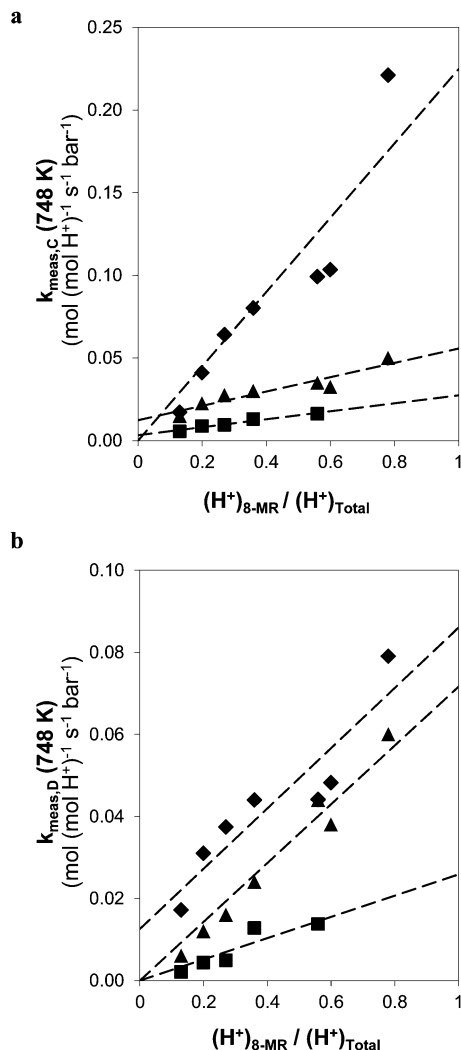


Fig. 5 Dependence of rate constants (per total H^+ ; 748 K) for monomolecular (a) cracking ($k_{\text{meas,C}}$) and (b) dehydrogenation ($k_{\text{meas,D}}$) of propane ($\times 20$; \blacktriangle), *n*-butane (\blacksquare) and iso-butane (\blacklozenge) on the fraction of 8-MR H^+ sites in MOR zeolites. Adapted from Gounder *et al.*⁷⁷

n- C_4H_{10} and for cracking of iso- C_4H_{10} on 12-MR H^+ sites.^{56,77} The higher turnover rates (per H^+) within 8-MR pockets than within 12-MR channels (*e.g.*, C_3H_8 cracking, Table 4) reflect lower ΔG_{meas} values and specifically lower transition state free energies, because ΔG_{meas} values for both 8-MR and 12-MR locations are referenced to the same gaseous alkane reactant (Scheme 2). ΔG_{meas} values for C_3H_8 cracking were smaller within 8-MR side pockets, in spite of larger measured activation energies (by 13 kJ mol^{-1} ; Table 4), because activation entropies were less negative in 8-MR pockets than in 12-MR channels (by 26 $\text{J mol}^{-1} \text{K}^{-1}$; Table 4). Thus, C_3H_8 cracking transition states do not gain as much enthalpy, but also do not lose as much entropy, when confined partially within 8-MR side pockets as when fully contained within 12-MR channels.⁵⁶

Propane cracking ion-pairs differ in free energy when confined within 8-MR and 12-MR MOR voids (Table 4) predominantly because of differences in their solvation, in light of similar electrostatic interactions with conjugate $[\text{AlO}_4]^-$ anions

Table 4 Measured first-order rate constants ($k_{\text{meas,C}}$), activation energies ($E_{\text{meas,C}}$), activation entropies ($\Delta S_{\text{meas,C}}$) and activation free energies ($\Delta G_{\text{meas,C}}$) for monomolecular propane cracking on H^+ sites located within 8-MR and 12-MR voids of MOR zeolites (748 K); adapted from Gounder *et al.*⁵⁶

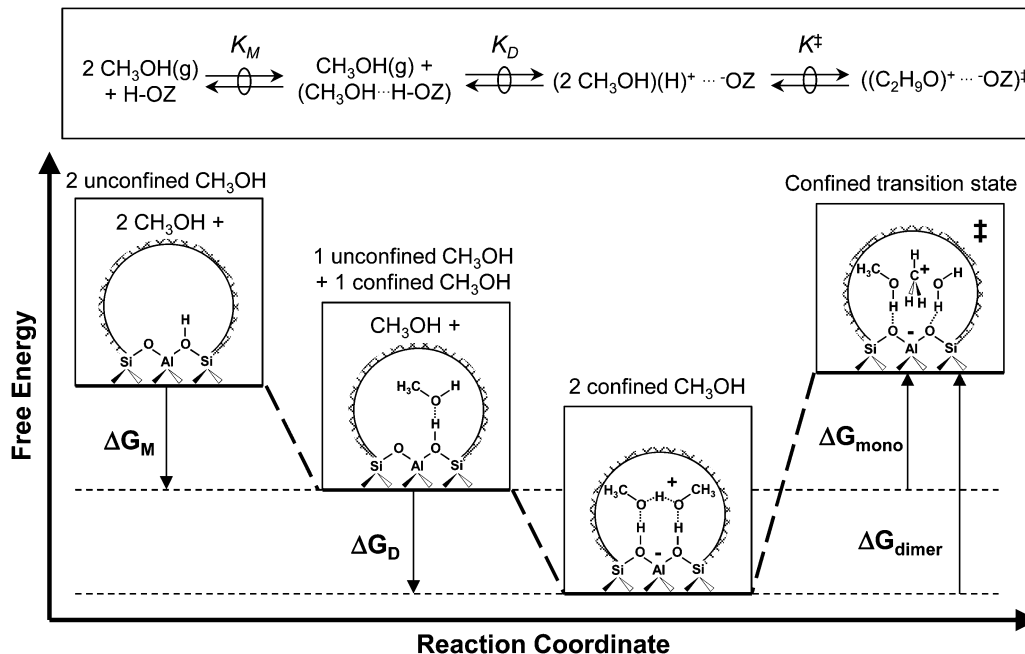
Location in MOR	$k_{\text{meas,C}}$ ($10^{-3} \text{ mol (mol } H^+)^{-1} \text{ s}^{-1} \text{ bar}^{-1}$)	$E_{\text{meas,C}}$ (kJ mol^{-1})	$\Delta S_{\text{meas,C}}$ ($\text{J mol}^{-1} \text{K}^{-1}$)	$\Delta G_{\text{meas,C}}$ (kJ mol^{-1})
8-MR side pockets	2.0 ± 0.5	164 ± 5	-91 ± 9	227 ± 2
12-MR channels	0.7 ± 0.4	151 ± 5	-117 ± 14	234 ± 3

at both locations, expected from the similar DPE values at 8-MR and 12-MR sites.³⁰ The solvation of cracking ion-pairs within 8-MR MOR pockets would mimic that of reactant alkanes of similar size and composition, but propane adsorption is detectable only within 12-MR MOR channels in low temperature (323 K) experiments.⁴⁶ Thus, we have estimated the ΔH_{ads} (-28 kJ mol^{-1}) and ΔS_{ads} ($-57 \text{ J mol}^{-1} \text{K}^{-1}$) values for partial confinement of C_3H_8 within 8-MR pockets from the values for C_3H_8 adsorption in 12-MR MOR channels ($\Delta H_{\text{ads}} = -41 \text{ kJ mol}^{-1}$; $\Delta S_{\text{ads}} = -85 \text{ J mol}^{-1} \text{K}^{-1}$),⁴⁶ by assuming that ΔH and ΔS differences between C_3H_8 cracking ion-pairs confined in 8-MR and 12-MR MOR voids (determined from the E_{meas} and ΔS_{meas} values in Table 4) were similar for the reactant alkanes. This assumption seems reasonable, to a first approximation, because the ΔH_{ads} and ΔS_{ads} values estimated for partial C_3H_8 confinement within 8-MR pockets resemble those predicted by the correlation between ΔH_{ads} and ΔS_{ads} values measured experimentally for full confinement in H-FER, H-MFI, H-MOR channels (Fig. 2).⁴⁴⁻⁴⁶ The less effective van der Waals stabilization of C_3H_8 molecules confined partially within shallow 8-MR MOR pockets than of those contained within larger 12-MR channels, evident in the less negative ΔH_{ads} and ΔS_{ads} values estimated for partial confinement within 8-MR pockets (Fig. 2), is also consistent with low temperature (323 K) adsorption studies that confirm the stronger enthalpic stabilization of C_3H_8 reactants within 12-MR MOR channels.⁴⁶

The strong effects of void structure on monomolecular alkane cracking and dehydrogenation turnover rates (Fig. 5) reflect catalytic turnovers that occur on sparsely covered surfaces. As a result, measured turnover rates depend on first-order rate constants (eqn (1)), which reflect the free energies of confined transition states relative to unconfined alkanes (Scheme 2). In contrast, alkanol dehydration turnover rates can be measured on surfaces at both low and high coverages of intermediates and with concomitant rate constants that “sense” void structures to different extents, as we show next.

3.3. Alkanol dehydration rates on acidic zeolites: the catalytic consequences of confining the relevant reactive intermediates

Methanol dehydration to dimethyl ether (DME) occurs on Brønsted solid acids *via* quasi-equilibrated methanol adsorption onto H^+ to form monomers (K_M), equilibrated adsorption of a second methanol molecule to form co-adsorbed dimers (K_D), and rearrangement to protonated precursors (K_C ; not shown) that eliminate water and DME (k_{DME}) in



Scheme 4 Reaction scheme for dimer-mediated alkanol dehydration (shown for CH₃OH using transition state theory formalism), involving the quasi-equilibrated, sequential adsorption of two gaseous alkanol molecules onto Brønsted acid sites (H–OZ) to form adsorbed alkanol monomers and dimers, followed by kinetically-relevant elimination of water to form the ether product. Gibbs free energy versus reaction coordinate diagram shows that first-order (k_{mono}) and zero-order (k_{dimer}) rate constants reflect free energy differences between the same confined transition state and either one (ΔG_{mono}) or two (ΔG_{dimer}) confined alkanol moieties.

kinetically-relevant irreversible steps (Scheme 4).¹⁴ This dimer-mediated dehydration sequence leads to the turnover rate (per H⁺) equation:¹⁴

$$r = \frac{k_{\text{DME}} K_{\text{C}} K_{\text{D}} K_{\text{M}} P_{\text{CH}_3\text{OH}}^2}{K_{\text{M}} P_{\text{CH}_3\text{OH}} + K_{\text{D}} K_{\text{M}} P_{\text{CH}_3\text{OH}}^2} = \frac{k_{\text{DME}} K_{\text{C}} K_{\text{D}} P_{\text{CH}_3\text{OH}}}{1 + K_{\text{D}} P_{\text{CH}_3\text{OH}}} \quad (13)$$

in which $P_{\text{CH}_3\text{OH}}$ is the gaseous methanol pressure. This equation is consistent with the observed dependence of DME synthesis turnover rates (per H⁺) on CH₃OH pressure on polyoxometalate and zeolitic acids:¹⁴

$$r = \frac{k_{\text{mono,M}} P_{\text{CH}_3\text{OH}}}{1 + \left(\frac{k_{\text{mono,M}}}{k_{\text{dimer,M}}}\right) P_{\text{CH}_3\text{OH}}} \quad (14)$$

In eqn (14), $k_{\text{mono,M}}$ and $k_{\text{dimer,M}}$ represent measured first-order and zero-order methanol dehydration rate constants, respectively. Ethanol dehydration to diethyl ether (DEE) proceeds *via* a similar sequence of elementary steps within H-FER, H-MFI and 12-MR H-MOR voids that are large enough to contain ethanol dimers.⁹³

This rate equation (eqn (14)) and its mechanistic interpretation (eqn (13)) indicate that dimer-mediated dehydration prevails over pressures that cause changes in the identity of the most abundant surface intermediates (MASI). At low CH₃OH pressure, H⁺ sites are predominantly occupied by neutral CH₃OH monomers ($K_{\text{M}} P_{\text{CH}_3\text{OH}} \gg K_{\text{D}} K_{\text{M}} P_{\text{CH}_3\text{OH}}^2$) and turnover rates are proportional to CH₃OH pressure:

$$r = k_{\text{mono,M}} P_{\text{CH}_3\text{OH}} \quad (15)$$

Higher CH₃OH pressures cause CH₃OH dimers to become the MASI ($K_{\text{D}} K_{\text{M}} P_{\text{CH}_3\text{OH}}^2 \gg K_{\text{M}} P_{\text{CH}_3\text{OH}}$) and turnover rates to become independent of CH₃OH pressure:

$$r = k_{\text{dimer,M}} \quad (16)$$

Measured first-order and zero-order rate constants can be expressed in terms of rate and equilibrium constants for elementary steps (k_{DME} , K_{C} , K_{D}):

$$\begin{aligned} k_{\text{mono,M}} &= k_{\text{DME}} K_{\text{C}} K_{\text{D}} \\ &= (k_{\text{B}} T/h) \exp\left(-\left(\Delta G_{\ddagger}^{\circ} - \Delta G_{\text{CH}_3\text{OH}(\text{g})}^{\circ} - \Delta G_{\text{CH}_3\text{OH}\cdots\text{H}^+\text{Z}^-}^{\circ}\right)/RT\right) \end{aligned} \quad (17)$$

$$\begin{aligned} k_{\text{dimer,M}} &= k_{\text{DME}} K_{\text{C}} \\ &= (k_{\text{B}} T/h) \exp\left(-\left(\Delta G_{\ddagger}^{\circ} - \Delta G_{[\text{CH}_3\text{OH}\cdots\text{H}\cdots\text{CH}_3\text{OH}]^+\text{Z}^-}^{\circ}\right)/RT\right) \end{aligned} \quad (18)$$

Turnover rates on surfaces covered by CH₃OH monomers depend on $k_{\text{mono,M}}$ (eqn (15)), which reflects the free energy of the DME formation transition state with respect to one confined and one gaseous CH₃OH molecule (eqn (17)). Rates on surfaces covered by CH₃OH dimers depend on $k_{\text{dimer,M}}$ (eqn (16)), which reflects the free energy of the same DME formation transition state relative to a confined protonated dimer (eqn (18); Scheme 4). Thus, adsorbate surface coverages during alkanol dehydration determine the kinetic relevance of specific reactive intermediates. Equations analogous to those for dimer-mediated methanol dehydration (eqn (13)–(18)) show

Table 5 Methanol dehydration (433 K) first-order ($k_{\text{mono,M}}$) and zero-order ($k_{\text{dimer,M}}$) rate constants on acidic zeolites. Ethanol dehydration (368 K) first-order ($k_{\text{mono,E}}$) and zero-order ($k_{\text{dimer,E}}$) rate constants on acidic zeolites

Zeolite	$k_{\text{dimer,M}}$ (10^{-3} (mol DME) (mol H ⁺) ⁻¹ s ⁻¹)	$k_{\text{mono,M}}$ (10^{-3} (mol DME) (mol H ⁺) ⁻¹ s ⁻¹ (kPa CH ₃ OH) ⁻¹)	$k_{\text{dimer,E}}$ (10^{-5} (mol DEE) (mol H ⁺) ⁻¹ s ⁻¹)	$k_{\text{mono,E}}$ (10^{-5} (mol DEE) (mol H ⁺) ⁻¹ s ⁻¹ (kPa C ₂ H ₅ OH) ⁻¹)
H-USY ^a	4.1	0.94	—	—
H-BEA ^a	2.9	0.96	—	—
CD-HUSY ^a	3.8	0.28	—	—
H-MFI ^b	—	—	1.7	0.0316
H-MOR ^b	—	—	3.3	0.0103
H-FER ^b	—	—	1.3	0.0014

^a Determined from data reported by Gounder *et al.*⁹⁴ ^b Determined from data reported by Chiang *et al.*⁹³

that effective first-order ($k_{\text{mono,E}}$) and zero-order ($k_{\text{dimer,E}}$) rate constants for dimer-mediated ethanol dehydration reflect the free energy of DEE formation transition states relative to one confined and one gaseous C₂H₅OH molecule or to two confined C₂H₅OH molecules in dimers, respectively.

Values of $k_{\text{mono,M}}$ and $k_{\text{dimer,M}}$ (433 K) on BEA and on two FAU zeolites (H-USY, CD-HUSY),⁹⁴ together with values of $k_{\text{mono,E}}$ and $k_{\text{dimer,E}}$ (368 K) for MFI, 10-MR FER channels, and 12-MR MOR channels (derived from K_{D} and k_{DEE} values)⁹³ are shown in Table 5. Values of k_{dimer} depend weakly on void size (varied by factors of ~ 1.4 and ~ 2.5 for CH₃OH and C₂H₅OH, respectively, Table 5), because ether formation ion-pairs and protonated alkanol dimers (eqn (18), Scheme 4) are similar in size and composition and are therefore solvated to a similar extent by van der Waals forces.¹⁴ In contrast, k_{mono} values depend more strongly on void size (varied by factors of ~ 3.4 and ~ 25 for CH₃OH and C₂H₅OH, respectively, Table 5) because the larger transition states are preferentially solvated over smaller alkanol monomers (eqn (17), Scheme 4).¹⁴ The stronger sensitivity to void size of k_{mono} values for C₂H₅OH than CH₃OH (Table 5) appears to reflect the confinement of DEE formation transition states (~ 0.52 nm kinetic diameter for DEE)⁹⁵ within FER, MOR and MFI voids nearly commensurate in size (~ 0.5 – 0.7 nm diameter), and the confinement of DME formation transition states (~ 0.44 nm kinetic diameter for DME)⁹⁵ within much larger voids in BEA and FAU (~ 0.7 – 1.3 nm diameter).

Methanol dehydration data gave similar $k_{\text{dimer,M}}$ values (within a factor of ~ 1.1 ; Table 5) on FAU zeolites treated in water vapor at high temperatures (973–1273 K) to form ultrastable-Y zeolites containing extra-framework Al species (H-USY, < 1.3 nm diam.), and on FAU treated chemically with (NH₄)₂SiF₆ to remove any occluded extra-framework Al species (CD-HUSY, ~ 1.3 nm diam.).^{28,96–99} These similar $k_{\text{dimer,M}}$ values suggest that they contain protons of similar acid strength, instead of the ‘superacidic’ Brønsted sites claimed to form *via* electron donation to Lewis acidic extraframework Al species,^{28,29,100,101} these ‘superacid’ sites were invoked to interpret differences among turnover rates when such rates were normalized by XRD- and NMR-derived measurements of framework Al atoms, instead of by the number of protons that act as the catalytic site.⁹⁴ Ar adsorption isotherms and ¹²⁹Xe NMR chemical shifts suggest that dispersion forces are stronger within supercage voids of H-USY than of CD-HUSY, apparently because the former sample contains extraframework Al moieties that occlude void space.^{40,102}

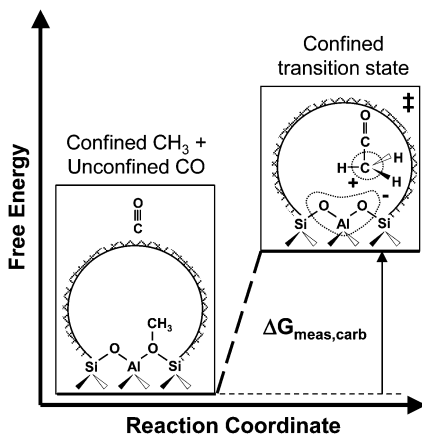
These observations suggest that methanol dehydration transition states are also more effectively solvated within smaller effective supercage voids in H-USY than in the larger voids of CD-HUSY, consistent with $k_{\text{mono,M}}$ values that are indeed higher for H-USY than CD-HUSY (by a factor of ~ 3.4 ; Table 5).

The different alkane activation⁹⁴ and alkanol dehydration⁹⁴ turnover rates on H-USY and CD-HUSY show that catalytic diversity prevails even among FAU structures, a framework with only one accessible void structure (~ 1.3 nm supercages) and a single T-site. These findings suggest that the *effective* void size, which reflects the framework structure only in part, determines how effectively guests are solvated by the host upon confinement. Other adsorbates or unreactive residues within void spaces, such as inorganic cations (K⁺, Na⁺ or Ca²⁺) in LTA zeolites (0.3, 0.4 or 0.5 nm in diameter, respectively) and inorganic or organic functional groups covalently grafted onto pore surfaces, can also modify the size and shape of the confining voids.¹⁰³ Thus, synthetic and post-synthetic methods that manipulate the *effective* void size provide opportunities to extend the range of solvating environments present within a given zeolite structure, a strategy that actually provides the sole option for structures that contain only a single crystallographic T-site or void environment.

3.4. Turnover rates for other reactions on MOR zeolites: when and how reactions sense void structure

We have shown how alkane activation and alkanol dehydration act as catalytic probes of void structure by informing about differences in the solvation of transition states relative to the relevant reactive intermediates, whose identity is dictated by the MASI prevalent during steady-state catalysis. Here, we expand this concept using the limiting case of dilute intra-zeolite concentrations of one or more reactants. In such cases, measured first-order rate constants depend on the free energy of the confined kinetically-relevant transition states relative to unconfined reactants, leading to strong effects of void structure on reactivity. We focus on MOR zeolites, because the location of protons is known, but the concepts are general.

The anhydrous carbonylation of DME to methyl acetate on zeolites occurs at lower temperatures (400–500 K) than alkane cracking or dehydrogenation (> 700 K). Carbonylation turnover rates (per Al) are proportional to CO pressure and independent of DME pressure,^{104,105} a kinetic behavior that reflects saturation coverages of DME-derived CH₃ groups



Scheme 5 Gibbs free energy versus reaction coordinate diagram for dimethyl ether carbonylation on a zeolitic acid shows that measured carbonylation rate constants ($k_{\text{meas,carb}}$) reflect the free energy of a confined $\text{CO}-\text{CH}_3^+$ transition state relative to one bound CH_3 group and one gaseous CO molecule ($\Delta G_{\text{meas,carb}}$).

and their kinetically-relevant reaction with CO molecules confined within void spaces.^{104,105} Carbonylation rates (per H^+) are given by:¹⁰⁵

$$r_{\text{carb}} = k_{\text{meas,carb}} P_{\text{CO}} \quad (19)$$

where $k_{\text{meas,carb}}$ is the measured carbonylation rate constant. This rate constant reflects the free energy of $(\text{CO}-\text{CH}_3)^+$ ion pairs at transition states confined within zeolitic voids ($\Delta G_{\ddagger}^{\circ}$) relative to those of a bound CH_3 group ($\Delta G_{\text{CH}_3^+}^{\circ}$) and a gaseous CO molecule ($\Delta G_{\text{CO(g)}}^{\circ}$) outside zeolite crystals (Scheme 5):

$$k_{\text{meas,carb}} = (k_{\text{B}}T/h) \exp\left(-\left(\Delta G_{\ddagger}^{\circ} - \Delta G_{\text{CO(g)}}^{\circ} - \Delta G_{\text{CH}_3^+}^{\circ}\right)/RT\right) \quad (20)$$

Thus, carbonylation rates should depend on void structure because confined $(\text{CO}-\text{CH}_3)^+$ transition states and CH_3 groups differ in size and composition and are stabilized to different extents upon confinement.

DME carbonylation turnover rates in MOR zeolites depend only on the number of protons within 8-MR side pockets (Fig. 6).⁸⁷ This enzyme-like specificity reflects lower activation barriers for backside attack of CO on CH_3 groups at 8-MR pockets (68 kJ mol^{-1} (MP2),¹⁰⁶ 52 kJ mol^{-1} (DFT-D)¹⁰⁷) than at 12-MR channels (93 kJ mol^{-1} (MP2),¹⁰⁶ 76 kJ mol^{-1} (DFT-D)¹⁰⁷). These theoretical treatments used MP2 and DFT-D methods, which include descriptions of attractive van der Waals interactions. Activation barriers become indistinguishable at 8-MR and 12-MR locations in MOR (76 and 79 kJ mol^{-1} ,¹⁰⁶ respectively) when using density functionals that neglect attractive dispersion forces, which are responsible for the solvation of confined moieties.

These data and theory show that van der Waals forces preferentially stabilize larger $(\text{CO}-\text{CH}_3)^+$ transition states over smaller CH_3 intermediates. Turnover rates are higher in 8-MR pockets, in spite of concomitant entropy losses, because of the preeminence of the enthalpy terms in Gibbs free energies (eqn (12)) at low temperatures (400–500 K).⁷⁰ In contrast,

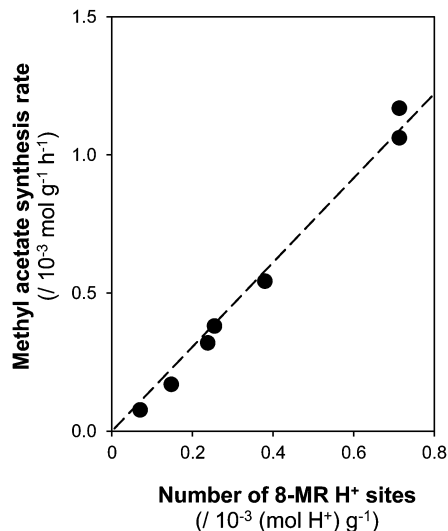


Fig. 6 Dependence of methyl acetate synthesis rates (per g; 438 K) during dimethyl ether carbonylation on the number of 8-MR H^+ sites (per g) in MOR zeolites. Adapted from Bhan *et al.*⁸⁷

alkane cracking and dehydrogenation turnover rates are higher in 8-MR pockets (Fig. 5), which confine only partially the transition states and lead to entropy gains (and concomitant losses in enthalpy), because entropy terms become preeminent at high temperatures (700–800 K).⁷⁰ Such effects of temperature on the relative importance of enthalpy and entropy terms in Gibbs free energy simply reflect the presence of temperature as a multiplier of entropy in eqn (12).

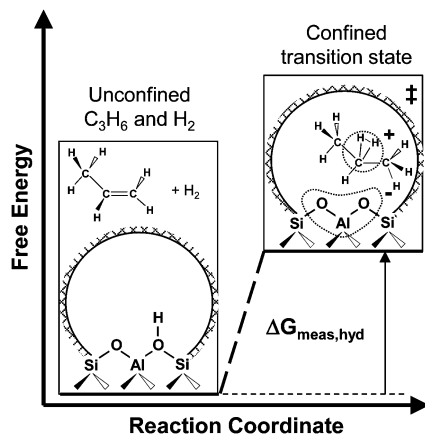
Acids catalyze alkene hydrogenation *via* the microscopic reverse of alkane dehydrogenation, which involves kinetically-relevant addition of intrazeolitic H_2 to bound alkoxides.⁹¹ Propene hydrogenation at high temperatures (700–800 K), low propene pressures (0.01–0.05 kPa), and excess H_2 (10–120 kPa) lead to sparsely covered surfaces and to turnover rates (per H^+) proportional to both propene ($P_{\text{C}_3\text{H}_6}$) and H_2 (P_{H_2}) pressures:⁹¹

$$r = k_{\text{meas,hyd}} P_{\text{C}_3\text{H}_6} P_{\text{H}_2} \quad (21)$$

Here, $k_{\text{meas,hyd}}$ reflects the free energy of $(\text{C}_3\text{H}_9)^+$ carbonium-ion-like transition states (also involved in C_3H_8 dehydrogenation) relative to unconfined H_2 and C_3H_6 molecules (Scheme 6), which are in quasi-equilibrium with the intrazeolitic H_2 and alkoxide reactive intermediates:⁹¹

$$k_{\text{meas,hyd}} = (k_{\text{B}}T/h) \exp\left(-\left(\Delta G_{\ddagger}^{\circ} - \Delta G_{\text{C}_3\text{H}_6(\text{g})}^{\circ} - \Delta G_{\text{H}_2(\text{g})}^{\circ} - \Delta G_{\text{H}^+}^{\circ}\right)/RT\right) \quad (22)$$

Propene hydrogenation rate constants (per total H^+) increased monotonically as the fraction of 8-MR H^+ sites in MOR zeolites increased, as in the case of propane dehydrogenation rate constants (Fig. 7).⁹¹ C_3H_6 hydrogenation transition states are preferentially stabilized by the entropic benefits of partial confinement within 8-MR side pockets, because they are the same as for C_3H_8 dehydrogenation. As a result, the $\Delta G_{\ddagger}^{\circ}$



Scheme 6 Gibbs free energy versus reaction coordinate diagram for alkene hydrogenation on a zeolitic acid (shown for C_3H_6) shows that measured rate constants ($k_{\text{meas,hyd}}$) reflect free energy differences between the hydrogenation transition state and an alkene and H_2 in the gas phase ($\Delta G_{\text{meas,hyd}}$).

term exactly cancels in the ratio of C_3H_8 dehydrogenation (eqn (6)) to C_3H_6 hydrogenation (eqn (22)) rate constants:

$$\begin{aligned} k_{\text{meas,D}}/k_{\text{meas,hyd}} \\ = \exp\left(-\left(\Delta G_{C_3H_6(g)}^{\circ} + \Delta G_{H_2(g)}^{\circ} - \Delta G_{C_3H_8(g)}^{\circ}\right)/RT\right) \end{aligned} \quad (23)$$

The free energy difference between products (C_3H_6 , H_2) and reactants (C_3H_8), which appears in eqn (23), is just the free energy of the interconversion of the gaseous reactants (ΔG_R°). This allows eqn (21) to be rewritten as:

$$k_{\text{meas,D}}/k_{\text{meas,hyd}} = \exp(-\Delta G_R^{\circ}/RT) = K_R \quad (24)$$

where K_R is the equilibrium constant for the overall reaction.⁹¹ The $k_{\text{meas,D}}/k_{\text{meas,hyd}}$ ratios on all zeolites were identical (within experimental accuracy) to K_R , irrespective of H^+ location in MOR zeolites (Fig. 7) or of zeolite topology (MFI, FER, MOR).⁹¹

Bound alkoxides can also undergo reactions with alkenes (dimerization),¹⁰⁸ with alkanes (alkylation),¹⁰⁸ and monomolecular β -scission¹⁰⁸ or isomerization.¹⁰⁹ Turnover rates for C_2H_4 dimerization and alkylation with CH_4 have been measured on sparsely covered surfaces at high temperatures (700–800 K), low alkene pressures (0–0.2 kPa C_2H_4) and high alkane pressures (0–200 kPa CH_4).¹⁰⁸ Dimerization rates are second-order in C_2H_4 pressure and alkylation rates are first-order in both C_2H_4 and CH_4 pressure:

$$r_{\text{dim}} = k_{\text{meas,dim}} P_{C_2H_4}^2 \quad (25)$$

$$r_{\text{alk}} = k_{\text{meas,alk}} P_{C_2H_4} P_{CH_4} \quad (26)$$

The rate constants for both reactions ($k_{\text{meas,dim}}$, $k_{\text{meas,alk}}$) depend on free energy differences between the respective confined transition state and unconfined reactants.¹⁰⁸ The values of $k_{\text{meas,dim}}$ and $k_{\text{meas,alk}}$ (per H^+) are higher in 8-MR pockets than in 12-MR channels,¹⁰⁸ because 8-MR pockets confine the respective transition states only partially, leading to larger entropies and smaller activation free energies at these temperatures (700–800 K). In fact, alkylation of C_2H_4 with CH_4 occurs *via* the microscopic reverse of monomolecular C_3H_8

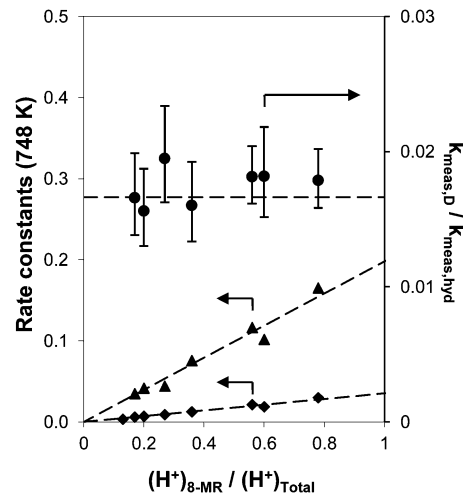


Fig. 7 Dependence of measured rate constants (per total H^+ ; 748 K) for monomolecular propane dehydrogenation ($k_{\text{meas,D}}$; $\times 10 \text{ mol (mol } H^+)^{-1} \text{ s}^{-1} (\text{bar } C_3H_8)^{-1}$; \blacklozenge) and propene hydrogenation ($k_{\text{meas,hyd}}$; $\text{mol (mol } H^+)^{-1} \text{ s}^{-1} (\text{bar } C_3H_6)^{-1} (\text{bar } H_2)^{-1}$; \blacktriangle), and of $k_{\text{meas,D}}/k_{\text{meas,hyd}}$ ratios (bar; \bullet), on the fraction of 8-MR H^+ sites in MOR zeolites. The equilibrium constant for the gas-phase propane dehydrogenation reaction ($K_R = 0.017 \text{ bar}$; 748 K) is given by the horizontal dashed line. Adapted from Gounder *et al.*⁹¹

cracking and at turnover rates limited by an elementary step that is identical but in the opposite direction, causing cracking-to-alkylation rate constant ratios to become independent of zeolite structure (FER, MFI, MOR) or acid site location (8-MR and 12-MR voids of MOR).¹⁰⁸ As for alkene dimerization and alkylation, first-order rate constants (per H^+) for β -scission¹⁰⁸ and isomerization¹⁰⁹ of alkoxides are also higher within 8-MR side pockets than 12-MR channels of MOR zeolites, because they reflect free energy differences between confined transition states and unconfined reactants.

Catalytic turnovers on zeolitic protons require confinement of reactants, formation of reactant-derived intermediates, and stabilization of ion-pair transition states. The rigorous mechanistic interpretations of alkane, alkene, alkanol and ether reactions discussed above show that when turnover rates are proportional to reactant pressures, unconfined reactants become kinetically-relevant while confined reactive intermediates become kinetically-irrelevant. Such turnover rates depend on void structure, which confine and solvate transition states but not extrazeolite reactants.

4. Consequences of void structure for catalytic selectivity: preferential solvation of a specific transition state structure

In Section 3, we have showed how turnover rates become sensitive to void structure when transition states are solvated to a different extent than the relevant intermediates. By extension, a confining void selectively catalyzes a given step among possible alternate paths when it preferentially solvates its transition state. Here, we examine parallel reactions of alkanes (cracking, dehydrogenation) and alkenes (methylation, isomerization, dimerization, β -scission, hydride transfer) on solid

acids to show how void structure and solvation influences selectivity.

4.1. Cracking and dehydrogenation selectivities in monomolecular alkane reactions: entropic discrimination among transition states of similar size

Alkanes undergo cracking and dehydrogenation *via* parallel monomolecular steps. Selectivity, in this context, reflects the ratio of their respective rate constants, which individually reflect free energy differences between their respective transition states and the common gaseous alkane reactant (eqn (6)). As a result, these rate constant ratios depend only on free energy differences between the transition states that mediate these two reactions:

$$k_{\text{meas,C}}/k_{\text{meas,D}} = \exp(-(\Delta G_{\ddagger,\text{C}}^{\circ} - \Delta G_{\ddagger,\text{D}}^{\circ})/RT) \quad (27)$$

Similarly, differences in measured cracking and dehydrogenation activation barriers (or entropies) merely reflect the corresponding enthalpy (or entropy) differences:

$$E_{\text{meas,C}} - E_{\text{meas,D}} = \Delta H_{\ddagger,\text{C}}^{\circ} - \Delta H_{\ddagger,\text{D}}^{\circ} \quad (28)$$

$$\Delta S_{\text{meas,C}} - \Delta S_{\text{meas,D}} = \Delta S_{\ddagger,\text{C}}^{\circ} - \Delta S_{\ddagger,\text{D}}^{\circ} \quad (29)$$

Yet, differences between cracking and dehydrogenation activation barriers for a given alkane do not depend on zeolite structure (FAU, FER, MFI, MOR; Fig. 4, Section 2.3), indicating that the two transition states (similar in size and composition) are enthalpically stabilized to a similar extent (eqn (28)) by van der Waals forces, irrespective of the confining environment. This suggests that any effects of void structure on selectivity would require that entropies for dehydrogenation and cracking transition states be affected differently by confinement.

Cracking-to-dehydrogenation rate constant ratios decreased for linear alkanes (C_3H_8 , $n\text{-C}_4\text{H}_{10}$) and increased for branched alkanes (iso- C_4H_{10}) as protons were preferentially located within 8-MR MOR pockets (Fig. 8).^{56,77} These selectivity differences reflect lower free energies (eqn (27)) for n -alkane dehydrogenation and iso-alkane cracking transition states, relative to their respective cracking and dehydrogenation counterparts, when confined within 8-MR MOR pockets instead of 12-MR channels. Activation barriers and transition state enthalpies (*via* eqn (28)) were higher for n -alkane dehydrogenation (relative to cracking) and for iso-alkane cracking (relative to dehydrogenation) on all zeolites (FAU, FER, MFI, MOR; Fig. 4), reflecting the less exothermic protonation of C-H and C-C bonds in gaseous n -alkane and iso-alkane reactants, respectively (eqn (11), Fig. 4). The higher energy transition states for n -alkane dehydrogenation and iso-alkane cracking also occur later along the reaction coordinate and involve looser ion-pair structures than their cracking and dehydrogenation analogs, respectively.^{110,111}

Thus, n -alkane dehydrogenation and iso-alkane cracking, mediated by later and looser ion-pairs relative to their respective cracking and dehydrogenation paths, appear to benefit preferentially from the entropy gains associated with partial confinement (eqn (29)).⁷⁷ Transition state entropies become preminent in determining activation free energies (eqn (12)) and turnover rates at the high temperatures of alkane activation

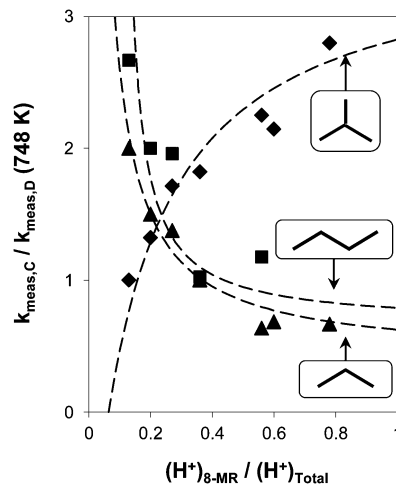


Fig. 8 Dependence of monomolecular cracking-to-dehydrogenation rate constant ratios (748 K) for propane (▲), n -butane (■) and iso-butane (◆) on the fraction of 8-MR H^+ sites in MOR zeolites. Dashed curves represent rate ratios predicted using rate constants on 8-MR and 12-MR sites reported by Gounder *et al.*^{56,77} Adapted from Gounder *et al.*⁷⁰

catalysis (700–800 K).⁷⁰ As a result, entropic differences between transition states (eqn (29)) become the dominant descriptor of activation free energies (eqn (27)) and of catalytic selectivity.

The relative cracking rates of different C–C bonds in alkane reactants define a positional cracking selectivity. The ratio of cracking rates for terminal and central C–C bonds in $n\text{-C}_4\text{H}_{10}$ increased as protons were preferentially located within 8-MR pockets in MOR (Fig. 9),⁵⁶ even though the transition states required to cleave these two C–C bonds are similar in size. These data reflect the partial confinement of n -alkanes within 8-MR side pockets, where acid sites preferentially access terminal over central C–C bonds.⁵⁶ This behavior is reminiscent of processes typically associated with ‘pore mouth’ catalysis,¹¹² which have been used to describe reactions of molecules that partially enter the confined spaces where active sites reside.

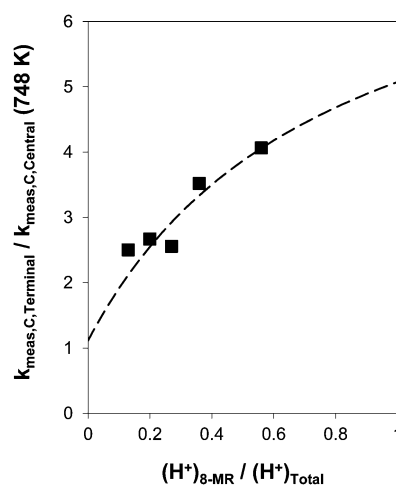
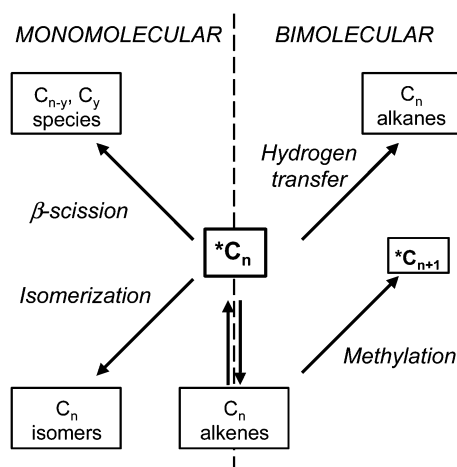


Fig. 9 Dependence of terminal-to-central C–C bond cracking rate constant ratios (748 K) for n -butane on the fraction of 8-MR H^+ sites in MOR zeolites. The dashed curve represent rate ratios predicted using rate constants on 8-MR and 12-MR sites reported by Gounder *et al.*⁵⁶

The different alkane cracking-to-dehydrogenation (Fig. 8) and terminal-to-central C–C bond cracking (Fig. 9) ratios in 8-MR and 12-MR MOR locations reflect differences in the lateness of or access to protons for the two transition states. These examples highlight how confining voids influence selectivity even when competing reactions are mediated by transition states of similar size and composition and when voids do not discern precisely among transition states based on enthalpy. Next, we show how confining voids are indeed able to influence selectivity *via* enthalpic stability when parallel reaction paths are mediated by transition states that differ in size or shape.

4.2. Selectivities in dimethyl ether homologation and alkene oligomerization reactions: enthalpic discrimination among transition states of different size or shape

Dimethyl ether homologation on solid Brønsted acids (400–500 K) involves the methylation of C_{n-1} alkenes by DME-derived adsorbed C_1 species to form C_n homologs, which can desorb to form a C_n alkane, undergo subsequent methylations, isomerize to a C_n intermediate with a different backbone, or desorb to form a C_n alkane upon hydride transfer from a H-donor (Scheme 7).^{113,114} Methylation of C_n ($n < 7$) intermediates occurs in positions that form the most stable carbenium-ion at transition states, which tend to preserve a four-carbon backbone.^{113,114} As a result, homologation paths preferentially form intermediates that act as precursors to 2,2,3-trimethylbutane (triptane).¹¹³ Isotopic studies showed that growing chains can methylate further to C_{8+} intermediates, which undergo facile β -scission (Scheme 7) to form iso-butane, as well as smaller alkenes that re-enter chain growth cycles.¹¹³ Chains also undergo skeletal isomerization to form intermediates that do not lead to triptane *via* subsequent methylation.¹¹³ Triptane and iso-butane are the preferred termination products of DME homologation and form *via* methylation events that preserve a four-carbon backbone; their selectivity increases with increasing methylation and hydride transfer rates and with decreasing isomerization rates.¹¹³



Scheme 7 Monomolecular and bimolecular reaction pathways of surface alkoxides ($*C_n$) and alkenes formed as intermediates during dimethyl ether homologation pathways on solid acids. Adapted from Simonetti *et al.*¹¹³

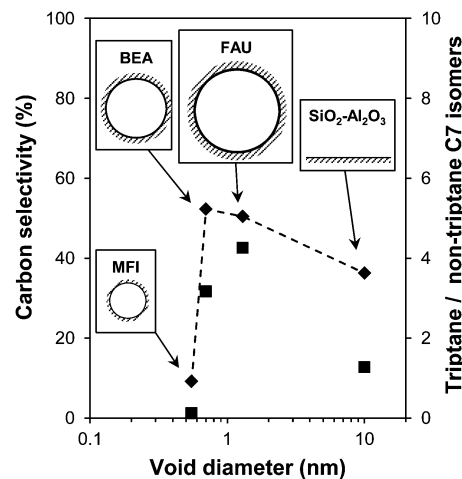


Fig. 10 Carbon selectivity to iso-butane and triptane (\blacklozenge) and the triptane/non-triptane isomer ratio in C_7 products (\blacksquare) formed during DME homologation (473 K) plotted as a function of approximate void diameter in MFI, BEA, FAU and $SiO_2-Al_2O_3$ solid acids. Data reported by Simonetti *et al.*¹¹⁵

DME homologation selectivities to triptane and iso-butane and triptane-to-non-triptane C_7 isomer ratios (473 K)¹¹⁵ are shown in Fig. 10 as a function of approximate void diameter on MFI (~ 0.55 nm), BEA (~ 0.70 nm) and FAU (~ 1.3 nm) and on amorphous $SiO_2-Al_2O_3$ (~ 10 nm). Triptane and iso-butane selectivities increase monotonically with decreasing void size ($SiO_2-Al_2O_3$, FAU and BEA; 0.7–10 nm diameter) and are much higher than on MFI (~ 0.55 nm diameter) (Fig. 10). These data suggest that methylation and hydride transfer of C_n intermediates become favored over isomerization within smaller voids, until the larger bimolecular transition states required for hydrogen transfer no longer fit within MFI channels.¹¹⁵ Larger bimolecular methylation and hydride-transfer transition states are preferentially stabilized by enthalpy over smaller ones for monomolecular isomerization upon confinement within a given void.¹¹⁵ At the low DME homologation temperatures (< 500 K), enthalpic stabilization prevails over concomitant entropy losses upon confinement, leading to higher triptane and iso-butane selectivities as voids decrease in size.

5. Outlook and conclusions: the catalytic diversity of microporous solid acids

The manner by which voids of molecular size enforce reaction specificity *via* confinement of transition states in zeolites is reminiscent of concepts broadly used to rationalize reactivity and selectivity in catalysis by enzymes^{6,8} and by imprinted solids.⁷ Such forms of transition state selectivity reflect the selective stabilization, by dispersion forces, of transition states that represent the “right fit” within certain “pockets” or voids; they contrast coarser-grained heuristics based on size exclusion, which tend to prevail in typical discourses of zeolite reactivity. The refinement of these concepts will require rigorous theoretical methods to assess the thermodynamics of adsorbed species and transition states,¹¹⁶ with special attention to the handling of attractive dispersion forces¹⁰⁶ that are neglected in

certain density functional-based methods. Such refinements will undoubtedly sharpen the tools by which we design and select voids with solvation properties specifically suited for a given transition state, an essential complement to the methods by which zeolite voids are chosen to control the access and egress of reactants and products using notions of shape selectivity and molecular traffic control,^{112,117–121} and to protect active sites from contact with toxic impurities.¹²²

5.1. Classical concepts in shape selectivity: the role of pore and aperture size

A historical emphasis on the size and shape of voids and of their connecting apertures has led to the emergence of probes, such as the constraint index,¹²⁴ and spaciousness index,¹²⁵ based on reactions of molecules of different size. These methods can indirectly assess the structural properties of new microporous solids¹²⁶ and are useful descriptors of reactivity when it is controlled by molecular transport or size exclusion. For instance, the constraint index (CI), defined as the ratio of *n*-hexane and 3-methylpentane cracking rates, increases as smaller channels obstruct the diffusion of the larger isomer.¹²³ CI values are different for frameworks limited by the same aperture size (10-MR) that contain (EUO, MWW, STF) or do not contain (MFI, MTT, TON) internal pockets or cages of larger dimensions.¹²⁷ CI values also increase in MOR with time-on-stream as unreactive residues selectively deactivate H⁺ sites within 12-MR channels over those in smaller 8-MR pockets.¹²⁸ Thus, the CI test and other probe reactions designed primarily to sense differences in limiting aperture size and void connectivity through their effects on molecular transport can also provide inferences about the diversity conferred by internal void features (*e.g.*, pockets, cages).

Shape selectivity concepts were demonstrated early in the history of zeolite acid catalysis^{129,130} and have since inspired and sustained many discoveries of novel zeolite frameworks and driven the engineering of hierarchical porous architectures and of the size and habit of zeolite crystals. The diversity of void geometries, topologies and connectivities within hypothetical zeolite frameworks ($\sim 10^6$ in number)^{131–133} and even within known synthetic zeolites ($\sim 10^2$)⁸⁰ is remarkable. Curiously, new zeolites deployed in commercial practice have relied largely on modifications of few ($\sim 10^1$) known zeolites,¹²¹ at least in part because of the ambiguity in using heuristic size exclusion principles to discriminate zeolites with similar void architectures, but also because of the challenges of discovering, formulating, and developing truly novel structures.¹²¹

In the following section, we conclude by discussing how a given zeolite structure, which often contains many solvating environments, already provides a great deal of unexploited diversity, with the potential to expand in very significant ways the suite of catalytic materials relevant to industrial practice.

5.2. Transition state selectivity revisited: the roles of confinement and solvation

Zeolite voids stabilize transition states with the “right fit”, allowing their architectural diversity to enforce a remarkable

range of reactivity and selectivity in spite of acid strength that is essentially the same among isolated Al atoms in different frameworks³⁴ or T-site locations in aluminosilicates.^{30–32} The catalytic consequences of void size in insulating microporous aluminosilicates are reminiscent of the effects of cluster size in semiconducting oxides³⁷ and metal clusters¹³⁴ of a given composition. The resulting non-uniformity of reactivity among diverse voids within a given framework structure is reminiscent of that present at metal surfaces,^{135,136} which reflects differences in coordination number or vicinal adsorbates^{137,138} and leads to “structure sensitivity”.¹³⁴ Whether on acids or metals, turnover rates sense local structure only when it stabilizes transition states and the *relevant* reactive intermediates to different extents.

Each zeolite framework contains diverse solvating environments, the geometric features of which can be appreciated using visualization tools,^{81,139,140} shape-selective adsorptive or catalytic probes,¹²⁶ or theoretical assessments of adsorption and diffusion of guest molecules.^{116,141} These methods, even when rigorously applied, cannot fully assess reactivity without more precise determination of proton locations, which remain a challenge even when Al positions are known, because the fraction of Al sites that retain protons during thermal treatment and catalysis is seldom accessible to experimentation.

These concepts and conclusions suggest strategies for the design of *reactive* volumes for specific catalytic purposes. One approach seeks to place or retain protons within specific voids, either by selective Al positioning during synthesis or thermal treatments,⁸² or by selective titration of protons at certain locations after synthesis (*e.g.*, Na⁺ exchange in MOR zeolites).^{87,89,92} Structure-directing agents can position Al atoms at specific T-sites during FER hydrothermal synthesis¹⁴² and cause systematic variations in the number of protons in 8-MR and 10-MR channels^{143–145} and in DME carbonylation turnover rates,¹⁴⁶ which require protons in 8-MR channels.⁸⁷ Another strategy seeks to tune solvation properties *via* post-synthesis exchange or deposition of inert guests that partially occlude void space (*e.g.*, extraframework Al moieties in FAU supercages),⁹⁴ an approach especially useful for frameworks that contain only a single T-site or void environment.

The examples discussed herein show how transition state selectivity is enforced by solvation within confining voids,^{12,70} and how such effects prevail over minor differences in acid strength among protons in zeolites, even though the latter are often invoked imprecisely and non-rigorously to explain reactivity and selectivity differences. We expect that a more rigorous appreciation of the consequences of solvation effects in catalysis, their intellectual distinction from weaker effects of acid strength, and the emergence of theoretical treatments that capture attractive dispersion forces will inspire more systematic approaches to tune the solvation properties of confining voids during synthesis and *via* post-synthesis structural modifications. New efforts to tailor the distribution of reactive volumes within a given zeolite structure would complement ongoing efforts to discover novel framework structures, thereby expanding further the catalytic diversity potentially available among microporous solids.

Acknowledgements

We acknowledge Prof. Aditya Bhan (Univ. of Minnesota), Dr Robert Carr, Mr Andrew Jones, Dr Josef Macht, Prof. Matthew Neurock (Univ. of Virginia), Dr Dante Simonetti, Dr Glenn Sunley (BP), and Dr Stacey Zones (Chevron) for their technical and conceptual contributions to the findings described in this perspective article and in previous studies jointly published and cited herein. The financial support from BP, p.l.c. and from the Chevron Energy Technology Company for the research described here is also gratefully acknowledged.

References

- P. B. Venuto, *Microporous Mater.*, 1994, **2**, 297–411.
- A. Corma, *Chem. Rev.*, 1995, **95**, 559–614.
- K. Tanabe and W. F. Holderich, *Appl. Catal., A*, 1999, **181**, 399–434.
- W. Vermeiren and J. P. Gilson, *Top. Catal.*, 2009, **52**, 1131–1161.
- C. Martinez and A. Corma, *Coord. Chem. Rev.*, 2011, **255**, 1558–1580.
- D. E. Koshland, *Proc. Natl. Acad. Sci. U. S. A.*, 1958, **44**, 98–104.
- M. E. Davis, A. Katz and W. R. Ahmad, *Chem. Mater.*, 1996, **8**, 1820–1839.
- A. D. Mesecar, B. L. Stoddard and D. E. Koshland, *Science*, 1997, **277**, 202–206.
- R. Lobo, *AIChE J.*, 2008, **54**, 1402–1409.
- V. B. Kazansky, *Acc. Chem. Res.*, 1991, **24**, 379–383.
- R. A. van Santen and G. J. Kramer, *Chem. Rev.*, 1995, **95**, 637–660.
- A. Bhan and E. Iglesia, *Acc. Chem. Res.*, 2008, **41**, 559–567.
- J. Macht, R. T. Carr and E. Iglesia, *J. Am. Chem. Soc.*, 2009, **131**, 6554–6565.
- R. T. Carr, M. Neurock and E. Iglesia, *J. Catal.*, 2011, **278**, 78–93.
- J. Sauer and M. Sierka, *J. Comput. Chem.*, 2000, **21**, 1470–1493.
- D. Farcasiu and A. Ghenciu, *Prog. Nucl. Magn. Reson. Spectrosc.*, 1996, **29**, 129–168.
- R. J. Gorte, *Catal. Lett.*, 1999, **62**, 1–13.
- W. E. Farneth and R. J. Gorte, *Chem. Rev.*, 1995, **95**, 615–635.
- D. J. Parrillo and R. J. Gorte, *J. Phys. Chem.*, 1993, **97**, 8786–8792.
- D. J. Parrillo, C. Lee, R. J. Gorte, D. White and W. E. Farneth, *J. Phys. Chem.*, 1995, **99**, 8745–8749.
- A. Chatterjee, T. Iwasaki, T. Ebina and A. Miyamoto, *Microporous Mesoporous Mater.*, 1998, **21**, 421–428.
- S. P. Yuan, J. G. Wang, Y. W. Li and H. J. Jiao, *J. Phys. Chem. A*, 2002, **106**, 8167–8172.
- R. Zhradnik, P. Hobza, B. Wichterlova and J. Cejka, *Collect. Czech. Chem. Commun.*, 1993, **58**, 2474–2488.
- B. Hunger, M. Heuchel, L. A. Clark and R. Q. Snurr, *J. Phys. Chem. B*, 2002, **106**, 3882–3889.
- W. O. Haag, *Zeolites and Related Microporous Materials: State of the Art 1994*, Elsevier Science Publ. B.V., Amsterdam, 1994, pp. 1375–1394.
- W. O. Haag, R. M. Lago and P. B. Weisz, *Nature*, 1984, **309**, 589–591.
- D. H. Olson, W. O. Haag and R. M. Lago, *J. Catal.*, 1980, **61**, 390–396.
- D. Barthomeuf, *Mater. Chem. Phys.*, 1987, **17**, 49–71.
- D. Barthomeuf and R. Beaumont, *J. Catal.*, 1973, **30**, 288–297.
- M. Brändle and J. Sauer, *J. Am. Chem. Soc.*, 1998, **120**, 1556–1570.
- C. Lo and B. L. Trout, *J. Catal.*, 2004, **227**, 77–89.
- U. Eichler, M. Brändle and J. Sauer, *J. Phys. Chem. B*, 1997, **101**, 10035–10050.
- P. Strodel, K. M. Neyman, H. Knözinger and N. Rosch, *Chem. Phys. Lett.*, 1995, **240**, 547–552.
- M. Sierka, U. Eichler, J. Datka and J. Sauer, *J. Phys. Chem. B*, 1998, **102**, 6397–6404.
- J. Macht, R. T. Carr and E. Iglesia, *J. Catal.*, 2009, **264**, 54–66.
- M. J. Janik, J. Macht, E. Iglesia and M. Neurock, *J. Phys. Chem. C*, 2009, **113**, 1872–1885.
- J. Macht and E. Iglesia, *Phys. Chem. Chem. Phys.*, 2008, **10**, 5331–5343.
- J. Macht, M. J. Janik, M. Neurock and E. Iglesia, *Angew. Chem., Int. Ed.*, 2007, **46**, 7864–7868.
- E. G. Derouane and M. E. Davis, *J. Mol. Catal.*, 1988, **48**, 37–41.
- R. L. Cotterman, D. A. Hickson, S. Cartledge, C. Dybowski, C. Tsiao and A. F. Venero, *Zeolites*, 1991, **11**, 27–34.
- P. J. Barrie and J. Klinowski, *Prog. Nucl. Magn. Reson. Spectrosc.*, 1992, **24**, 91–108.
- P. E. Hathaway and M. E. Davis, *Catal. Lett.*, 1990, **5**, 333–348.
- S. Savitz, F. Siperstein, R. J. Gorte and A. L. Myers, *J. Phys. Chem. B*, 1998, **102**, 6865–6872.
- F. Eder and J. A. Lercher, *J. Phys. Chem. B*, 1997, **101**, 1273–1278.
- F. Eder and J. A. Lercher, *Zeolites*, 1997, **18**, 75–81.
- F. Eder, M. Stockenhuber and J. A. Lercher, *J. Phys. Chem. B*, 1997, **101**, 5414–5419.
- F. Eder and J. A. Lercher, *J. Phys. Chem.*, 1996, **100**, 16460–16462.
- J. F. Denayer, G. V. Baron, J. A. Martens and P. A. Jacobs, *J. Phys. Chem. B*, 1998, **102**, 3077–3081.
- J. F. Denayer, W. Souverijns, P. A. Jacobs, J. A. Martens and G. V. Baron, *J. Phys. Chem. B*, 1998, **102**, 4588–4597.
- C. E. Ramachandran, B. A. Williams, J. A. van Bokhoven and J. T. Miller, *J. Catal.*, 2005, **233**, 100–108.
- C. C. Lee, R. J. Gorte and W. E. Farneth, *J. Phys. Chem. B*, 1997, **101**, 3811–3817.
- E. E. Mallon, A. Bhan and M. Tsapatsis, *J. Phys. Chem. B*, 2010, **114**, 1939–1945.
- E. E. Mallon, I. J. Babineau, J. I. Kranz, Y. Guefrachi, J. I. Siepmann, A. Bhan and M. Tsapatsis, *J. Phys. Chem. B*, 2011, **115**, 11431–11438.
- G. C. Bond, M. A. Keane, H. Kral and J. A. Lercher, *Catal. Rev. Sci. Eng.*, 2000, **42**, 323–383.
- W. O. Haag and R. M. Dessau, *Proc. 8th Int. Congr. Catalysis*, Berlin, 1984, vol. 2, pp. 305–316.
- R. Gounder and E. Iglesia, *J. Am. Chem. Soc.*, 2009, **131**, 1958–1971.
- M. T. Aronson, R. J. Gorte and W. E. Farneth, *J. Catal.*, 1986, **98**, 434–443.
- J. Macht, M. J. Janik, M. Neurock and E. Iglesia, *J. Am. Chem. Soc.*, 2008, **130**, 10369–10379.
- S. J. Collins and P. J. O'Malley, *Top. Catal.*, 1998, **6**, 151–161.
- P. M. Esteves, C. J. A. Mota, A. Ramirez-Solis and R. Hernández-Lamonedá, *J. Am. Chem. Soc.*, 1998, **120**, 3213–3219.
- P. M. Esteves, G. G. P. Alberto, A. Ramirez-Solis and C. J. A. Mota, *J. Phys. Chem. A*, 2000, **104**, 6233–6240.
- C. J. A. Mota, P. M. Esteves, A. Ramirez-Solis and R. Hernández-Lamonedá, *J. Am. Chem. Soc.*, 1997, **119**, 5193–5199.
- S. A. Zygmunt, L. A. Curtiss, P. Zapol and L. E. Iton, *J. Phys. Chem. B*, 2000, **104**, 1944–1949.
- X. B. Zheng and P. Blowers, *J. Phys. Chem. A*, 2005, **109**, 10734–10741.
- X. B. Zheng and P. Blowers, *J. Phys. Chem. A*, 2006, **110**, 2455–2460.
- V. B. Kazansky, M. V. Frash and R. A. van Santen, *Appl. Catal., A*, 1996, **146**, 225–247.
- T. F. Narbeshuber, H. Vinek and J. A. Lercher, *J. Catal.*, 1995, **157**, 388–395.
- K. C. Hunter and A. L. L. East, *J. Phys. Chem. A*, 2002, **106**, 1346–1356.
- J. Wei, *Chem. Eng. Sci.*, 1996, **51**, 2995–2999.
- R. Gounder and E. Iglesia, *Acc. Chem. Res.*, 2012, **45**, 229–238.
- D. X. Liu, A. Bhan, M. Tsapatsis and S. Al Hashimi, *ACS Catal.*, 2011, **1**, 7–17.
- B. Xu, C. Sievers, S. B. Hong, R. Prins and J. A. van Bokhoven, *J. Catal.*, 2006, **244**, 163–168.
- Y. J. He, G. S. Nivarthy, F. Eder, K. Seshan and J. A. Lercher, *Microporous Mesoporous Mater.*, 1998, **25**, 207–224.
- S. M. Babitz, B. A. Williams, J. T. Miller, R. Q. Snurr, W. O. Haag and H. H. Kung, *Appl. Catal., A*, 1999, **179**, 71–86.
- M. V. Frash and R. A. van Santen, *Top. Catal.*, 1999, **9**, 191–205.
- A. M. Rigby, G. J. Kramer and R. A. van Santen, *J. Catal.*, 1997, **170**, 1–10.
- R. Gounder and E. Iglesia, *Angew. Chem., Int. Ed.*, 2010, **49**, 808–811.
- A. Bhan, R. Gounder, J. Macht and E. Iglesia, *J. Catal.*, 2008, **253**, 221–224.
- J. Bandiera, M. Dufaux and Y. BenTaarit, *Appl. Catal., A*, 1997, **148**, 283–300.
- C. Baerlocher and L. B. McCusker, Database of Zeolite Structures, <http://www.iza-structure.org/databases/>.
- M. D. Foster, I. Rivin, M. M. J. Treacy and O. D. Friedrichs, *Microporous Mesoporous Mater.*, 2006, **90**, 32–38.
- J. Dedecek, Z. Sobalik and B. Wichterlova, *Catal. Rev. Sci. Eng.*, 2012, **54**, 135–223.
- S. Sklenak, J. Dedecek, C. Li, B. Wichterlova, V. Gabova, M. Sierka and J. Sauer, *Phys. Chem. Chem. Phys.*, 2009, **11**, 1237–1247.

- 84 S. Sklenak, J. Dedecek, C. B. Li, B. Wichterlova, V. Gabova, M. Sierka and J. Sauer, *Angew. Chem., Int. Ed.*, 2007, **46**, 7286–7289.
- 85 J. A. Van Bokhoven, T. L. Lee, M. Drakopoulos, C. Lamberti, S. Thiess and J. Zegenhagen, *Nat. Mater.*, 2008, **7**, 551–555.
- 86 G. Busca, *Chem. Rev.*, 2007, **107**, 5366–5410.
- 87 A. Bhan, A. D. Allian, G. J. Sunley, D. J. Law and E. Iglesia, *J. Am. Chem. Soc.*, 2007, **129**, 4919–4924.
- 88 J. Datka, B. Gil and A. Kubacka, *Zeolites*, 1997, **18**, 245–249.
- 89 M. Maache, A. Janin, J. C. Lavalley and E. Benazzi, *Zeolites*, 1995, **15**, 507–516.
- 90 M. A. Makarova, A. E. Wilson, B. J. vanLiemt, C. Mesters, A. W. deWinter and C. Williams, *J. Catal.*, 1997, **172**, 170–177.
- 91 R. Gounder and E. Iglesia, *J. Catal.*, 2011, **277**, 36–45.
- 92 V. A. Veeffkind, M. L. Smidt and J. A. Lercher, *Appl. Catal., A*, 2000, **194**, 319–332.
- 93 H. Chiang and A. Bhan, *J. Catal.*, 2010, **271**, 251–261.
- 94 R. Gounder, A. J. Jones, R. T. Carr and E. Iglesia, *J. Catal.*, 2012, **286**, 214–223.
- 95 M. E. van Leeuwen, *Fluid Phase Equilib.*, 1994, **99**, 1–18.
- 96 R. A. Beyerlein, G. B. McVicker, L. N. Yacullo and J. J. Ziemiak, *J. Phys. Chem.*, 1988, **92**, 1967–1970.
- 97 P. V. Shertukde, W. K. Hall, J. M. Dereppe and G. Marcelin, *J. Catal.*, 1993, **139**, 468–481.
- 98 J. R. Sohn, S. J. Decanio, P. O. Fritz and J. H. Lunsford, *J. Phys. Chem.*, 1986, **90**, 4847–4851.
- 99 B. Xu, S. Bordiga, R. Prins and J. A. van Bokhoven, *Appl. Catal., A*, 2007, **333**, 245–253.
- 100 R. A. Beyerlein, G. B. McVicker, L. N. Yacullo and J. J. Ziemiak, *Prepr. Am. Chem. Soc., Div. Pet. Chem.*, 1986, **190**, 197.
- 101 P. O. Fritz and J. H. Lunsford, *J. Catal.*, 1989, **118**, 85–98.
- 102 R. J. Pellet, C. S. Blackwell and J. A. Rabo, *J. Catal.*, 1988, **114**, 71–89.
- 103 E. F. Vansant, *Pore Size Engineering in Zeolites*, Wiley, New York, 1990.
- 104 P. Cheung, A. Bhan, G. J. Sunley and E. Iglesia, *Angew. Chem., Int. Ed.*, 2006, **45**, 1617–1620.
- 105 P. Cheung, A. Bhan, G. J. Sunley, D. J. Law and E. Iglesia, *J. Catal.*, 2007, **245**, 110–123.
- 106 M. Neurock, *Ind. Eng. Chem. Res.*, 2010, **49**, 10183–10199.
- 107 M. Boronat, C. Martinez and A. Corma, *Phys. Chem. Chem. Phys.*, 2011, **13**, 2603–2612.
- 108 R. Gounder and E. Iglesia, *ChemCatChem*, 2011, **3**, 1134–1138.
- 109 H. Chiang and A. Bhan, *J. Catal.*, 2011, **283**, 98–107.
- 110 R. P. Bell, *The Proton in Chemistry*, Chapman and Hall, London, 1973.
- 111 R. A. Marcus, *Annu. Rev. Phys. Chem.*, 1964, **15**, 155–196.
- 112 T. F. Degnan, *J. Catal.*, 2003, **216**, 32–46.
- 113 D. A. Simonetti, J. H. Ahn and E. Iglesia, *J. Catal.*, 2011, **277**, 173–195.
- 114 N. Hazari, E. Iglesia, J. A. Labinger and D. A. Simonetti, *Acc. Chem. Res.*, 2012, **45**, 653–662.
- 115 D. A. Simonetti, R. T. Carr and E. Iglesia, *J. Catal.*, 2012, **285**, 19–30.
- 116 B. Smit and T. L. M. Maesen, *Nature*, 2008, **451**, 671–678.
- 117 S. M. Csicsery, *Zeolites*, 1984, **4**, 202–213.
- 118 C. R. Marcilly, *Top. Catal.*, 2000, **13**, 357–366.
- 119 E. G. Derouane and Z. Gabelica, *J. Catal.*, 1980, **65**, 486–489.
- 120 S. M. Csicsery, *Pure Appl. Chem.*, 1986, **58**, 841–856.
- 121 S. I. Zones, *Microporous Mesoporous Mater.*, 2011, **144**, 1–8.
- 122 S. Goel, Z. J. Wu, S. I. Zones and E. Iglesia, *J. Am. Chem. Soc.*, 2012, **134**, 17688–17695.
- 123 V. J. Frillette, W. O. Haag and R. M. Lago, *J. Catal.*, 1981, **67**, 218–222.
- 124 J. A. Martens, M. Tielen, P. A. Jacobs and J. Weitkamp, *Zeolites*, 1984, **4**, 98–107.
- 125 J. Weitkamp, S. Ernst and R. Kumar, *Appl. Catal.*, 1986, **27**, 207–210.
- 126 S. I. Zones, C. Y. Chen, A. Corma, M. T. Cheng, C. L. Kibby, I. Y. Chan and A. W. Burton, *J. Catal.*, 2007, **250**, 41–54.
- 127 S. I. Zones and T. V. Harris, *Microporous Mesoporous Mater.*, 2000, **35–36**, 31–46.
- 128 J. R. Carpenter, S. Yeh, S. I. Zones and M. E. Davis, *J. Catal.*, 2010, **269**, 64–70.
- 129 P. B. Weisz and V. J. Frillette, *J. Phys. Chem.*, 1960, **64**, 382–382.
- 130 P. B. Weisz, V. J. Frillette, R. W. Maatman and E. B. Mower, *J. Catal.*, 1962, **1**, 307–312.
- 131 M. W. Deem, R. Pophale, P. A. Cheeseman and D. J. Earl, *J. Phys. Chem. C*, 2009, **113**, 21353–21360.
- 132 R. Pophale, P. A. Cheeseman and M. W. Deem, *Phys. Chem. Chem. Phys.*, 2011, **13**, 12407–12412.
- 133 M. M. J. Treacy, I. Rivin, E. Balkovsky, K. H. Randall and M. D. Foster, *Microporous Mesoporous Mater.*, 2004, **74**, 121–132.
- 134 M. Boudart, *Adv. Catal.*, 1969, **20**, 153–166.
- 135 H. S. Taylor, *Proc. R. Soc. Lond. Ser. A*, 1925, **108**, 105–111.
- 136 M. Boudart, *J. Am. Chem. Soc.*, 1950, **72**, 1040–1040.
- 137 M. Boudart, *J. Am. Chem. Soc.*, 1952, **74**, 1531–1535.
- 138 M. Boudart, *J. Am. Chem. Soc.*, 1952, **74**, 3556–3561.
- 139 M. M. J. Treacy and M. D. Foster, *Microporous Mesoporous Mater.*, 2009, **118**, 106–114.
- 140 E. L. First, C. E. Gounaris, J. Wei and C. A. Floudas, *Phys. Chem. Chem. Phys.*, 2011, **13**, 17339–17358.
- 141 E. Haldoupis, S. Nair and D. S. Sholl, *Phys. Chem. Chem. Phys.*, 2011, **13**, 5053–5060.
- 142 L. Gomez-Hortiguera, A. B. Pinar, F. Cora and J. Perez-Pariente, *Chem. Commun.*, 2010, **46**, 2073–2075.
- 143 A. B. Pinar, C. Marquez-Alvarez, M. Grande-Casas and J. Perez-Pariente, *J. Catal.*, 2009, **263**, 258–265.
- 144 A. B. Pinar, P. A. Wright, L. Gomez-Hortiguera and J. Perez-Pariente, *Microporous Mesoporous Mater.*, 2010, **129**, 164–172.
- 145 A. B. Pinar, R. Garcia, L. Gomez-Hortiguera and J. Perez-Pariente, *Top. Catal.*, 2010, **53**, 1297–1303.
- 146 Y. Román-Leshkov, M. Moliner and M. E. Davis, *J. Phys. Chem. C*, 2011, **115**, 1096–1102.